POLITECNICO DI TORINO

Collegio di Ingegneria Chimica e dei Materiali

Master of Science Course in Materials Engineering for Industry 4.0

Master of Science Thesis

Investigation of machining residual stress on fatigue life at the groove scale



Tutors Candidate

Pr. Frederic Valiorgue Prof. Daniele Ugues Prof. Cédric Bosch

Maldeniya Arachchige Don Sachintha Banuka Maldeniyaarachchi

September 2025

Abstract

Machining is a subtractive manufacturing method that eliminates materials and forms grooves with consecutive passes of a machined tool on machined surface. This machined induced surface integrity has a significant impact on the fatigue life of sectors like as aerospace and nuclear components, among others. Residual stress influences fatigue life on a global scale. However, MISULTECH's two-scale method to modelling 3D residual stresses indicates that a residual stress gradient exists on the machined surface. However, fatigue curves do not take these characteristics into consideration and instead assume that the surfaces are relaxed and completely smooth. And the effect of groove scale residual stress on fatigue life of machined components is a novel issue that has yet to be discovered. This innovative study was conducted to assess global and local residual stresses on the fatigue life of machined components.

Acknowledgments

I am incredibly grateful to the META 4.0 program, its coordinators (especially Prof. Cedric Courbon) and the program manager, Dr. Auralie Brayet, for providing me with the opportunity to have two of the most rewarding and demanding years of my life. Thanks to these classes, I've become a more self-assured and capable person. Thank you to everyone who has stuck with me over the past two years.

This incredible chance to learn about this fascinating subject is much appreciated by Team Misutech, and in particular by Professors Frederic Valiorgur and Professor Joel Rech. It means the world to me. In addition to Polly Loic, Dr. Marc Raffestin Thank you very much for all the help you've provided me with this project. For all the technical help I've had from LTDS, I'd like to thank Mr. Pascal Herve, Madam Jacquier Maryan, Dr. Viéville Emilie, and Mr. André Thierry. Outside of the topic matter, you have taught me a great deal. It means to me that people have shown me love, generosity, and hospitality. Additionally, I'd like to express my gratitude to Professor Etienne Pessard for his advice on this novel topic.

For all the love and support they've given me, my family my parents and two brothers are very much appreciated. My hometown pals, for making me laugh and smile while we sipped our cocktails. As always, I am grateful to my friends, but especially Thusira and Dewmini, for being there for me.

Table of Contents

Abstract		I
Acknowle	dgments	II
Table of C	ontents	III
Nomencla	ture	XI
Chapter 1	Introduction and Literature review	1
1.1. Mach	ining	1
1.2. Mach	ining induced surfaces and fatigue life	2
1.2.1.	Geometrical parameters	2
1.2.2.	Metallurgical parameters	4
1.2.3.	Mechanical parameters	5
1.3. Mode	elling of residual stresses induced by machining	8
1.3.1.	Modelling of Friction coefficient	13
1.4. Fatig	ue life	15
1.4.1.	Nomenclature for HCF	16
1.4.2.	Fatigue testing	19
1.5. Resea	arch gap and objectives	20
Chapter 2	Materials and Methods	21
2.1. Mate	rial properties	21
2.2. Expe	riment Protocol of sample preparation	25
2.3. Mate	rials Characterization	25
2.4. Heat	treatment	27
2.5. Tool	Characterization	28
2.6 Mach	ininσ	30

2.7. X Ray	Diffraction Measurement	32
2.7.1.	Bragg's law	32
2.8. Fatig	ue testing	33
Chapter 3	Machining	34
3.1. Tool (characterization	34
3.2. Cuttin	ng forces analysis	35
3.3. Geom	etrical surface state of the samples	35
3.4. Tool v	wear analysis	36
3.4.1.	Flank wear (Vb)	36
3.4.2.	Relief angle (α -Vb)	36
3.4.3.	Edge sharpness radius (ESR)	36
3.5. Mode	lling of Machining	37
3.5.1.	Modelling of machining of AISI 4140	37
3.5.2.	Modelling of machining of 316L SS	39
3.5.3.	Simulation results	40
3.5.4.	Modelling of Residual Stress	43
3.6. Theor	retical, Numerical and Experimental chip correlation	48
Chapter 4	Fatigue Testing and modelling	51
4.1. Cond	ucting fatigue experiments	51
4.1.1.	AISI 4140 machined samples testing	51
4.1.2.	AISI 4140 Machined then stress relieved samples testing	56
4.1.3.	316L SS machined and machined, stress relief annealed samples testing	57
4.1.4.	Failure points of AISI 4140	58
4.2. Critic	al distance analysis	58
Chapter 5	Discussion of Results	62
Chapter 6	Conclusion	67

Bibliography 68

List of Figures

Figure 1.1 Groove formation during machining2
Figure 1.2 Surface integrity maps of the fatigue samples of 15-5ph (Chomienne et al.
2023)3
Figure 1.3 Turning-induced microstructure gradient beneath the surface in the case of
longitudinal turning assessed by SEM (Dumas et al., 2021)4
Figure 1.4 Average residual stress profiles obtained for each manufacturing sequence for
15-5 PH (Chomienne et al., 2023)5
Figure 1.5 a) Surface integrity maps of the fatigue sample according to study conducted
by b) Correlation between fatigue strength and surface roughness c) Correlation
between fatigue strength and microstructure affected depth (Chomienne et al., 2023)6
Figure 1.6 Simplified thermos-mechanical loadings mentioned in the (Mondelin et al.
2012)9
Figure 1.7 Principle of the residual stress modelling based on a two-scale approach. a)
longitudinal turning operation, b) zoom on the chip formation zone, c) turning operation
modelling based on equivalent thermo-mechanical loadings (Mondelin et al., 2012), d
turning operation modelling based on new advanced equivalent thermo-mechanical
loadings (Aridhi et al., 2022)10
Figure 1.8 Flowchart of the new 3D hybrid methodology (Dumas, Fabre, et al., 2021b)
11
Figure 1.9 Final 3D equivalent thermo-mechanical loadings description with physical
shapes and corrected intensities. a) finite element model, b) heat flux density, c) normal
pressure d) tangential pressure (Dumas et al., 2021a)12
Figure 1.10 Field transfer procedure used for the modelling of several cutting tool
passages13
Figure 1.11 Numerical residual stress profiles building methodology, a) model
overlapping of successive revolutions, b) surface residual stress average on a stabilized
zone, c) in-depth average layer by layer for residual stress profile building (Dumas
Fabre, et al., 2021a)14
Figure 1.12 Wohler curve (Enomoto, 2022)15

Figure 1.13 Stress gradient of the notched specimen (Limodin & Verreman, 2006)) 17
Figure 1.14 Notch sensitivity for various materials (Vernon & Mackin, 2001)	19
Figure 2.1 Behavior of AISI 4140 obtained from Johnson-Cook parameters	23
Figure 2.2 Behavior of 316L stainless steel (Lurdos, 2008)	23
Figure 2.3 Experiment protocol for each material	25
Figure 2.4 Microstructure observation of AISI 4140 a) 10x and b) 50x	26
Figure 2.5 Microstructure observation of 316L a) 10x and b) 50x	26
Figure 2.6 Insert holder PDNRR 2020 15A B) Insert DNMG 150608 PF 4315 C)	DNMG
150608 QM 235	29
Figure 2.7 Engineering drawing of Fatigue simple	30
Figure 2.8 (a) Machine tool (b) Mounting of the sample to the lathe machine	31
Figure 2.9 XRD measurement of residual stress	32
Figure 2.10 a) Fatigue testing apparatus b) mounting of fatigue sample	33
Figure 3.1 Tool geometry terminology	34
Figure 3.2 Machining forces of AISI 4140 sample 5 b) Filtered machining forces	of thin
section of fatigue sample of AISI 4140 sample 5	35
Figure 3.3 Terminology used for describing tool wear	36
Figure 3.4 a) Orthogonal cutting operation performed for AISI 4140 for uncu	ıt chip
thickness $h(3)$ b) Heat flux density c) Tangential pressure d) Normal pressure ext	tracted
through extraction line	38
Figure 3.5 a) Orthogonal cutting operation performed for AISI 4140 for uncu	ıt chip
thickness $h(3)$ b) Heat flux density c) Tangential pressure d) Normal pressure ext	tracted
through extraction line	40
Figure 3.6 Temperature spreading a) AISI 4140 and b) 316L SS	41
Figure 3.7 Temperature stabilization a) AISI 4140 and b) 316L SS	42
Figure 3.8 Residual stress of 316L SS a) Cut stress b) Feed stress	43
Figure 3.9 Residual stress of AISI 4140 a) Cut stress b) Feed stress	44
Figure 3.10 Revolution number check a) for AISI 4140 b) for 316L SS	46
Figure 3.11 Mesh stabilization check	47
Figure 3.12 Chip sample collection of a) AISI 4140 b) 316L SS	48
Figure 3.13 Experiment chip section of a) AISI 4140 and b) 316L SS	48
Figure 3.14 Methodology of theoretical, numerical and experimental chip correlate	tion 49

Figure 4.1 Optical microscope observation of crack of AISI 414051
Figure 4.2 X ray profilometer scan of crack of AISI 4140 sample 352
Figure 4.3 Failure surface analysis of AISI 4140 a) sample 1 b) sample 252
Figure 4.4 Crack initiation sites of AISI 4140 a) b) sample 1, c) d) sample 253
Figure 4.5 Crack initiation site of AISI 4140 sample 354
Figure 4.6 EDS analysis of crack initiation site of AISI 4140 sample 155
Figure 4.7 Chemical composition of AISI 4140 simple 1
Figure 4.8 AISI 4140 TTH sample 6 Failure56
Figure 4.9 Crack propagation within the threads in AISI 4140 TTH sample $5\ldots57$
Figure 4.10 Failure points of AISI 4140
Figure 4.11 Pits observation of AISI 414059
Figure 4.12 Simulation methodology60
Figure 4.13 Stress gradient comparison with pits and without pits60
Figure 5.1 Microstructure of AISI 4140 machined a) surface b) bulk63
$Figure\ 5.2\ Microstructure\ of\ AISI\ 4140\ machined\ and\ stress\ relief\ annealed\ a)\ surface\ b)$
bulk63
Figure 5.3 Microstructure of 316L SS machined and stress relief annealed65
Figure 5.4 Microstructure of 316L SS of machined65

List of Tables

Table 1.1 Stress ratio common values and their interpretations	16
Table 2.1 Materials composition of AISI 4140 (Badaruddin et al., 2019) and	l 316L SS
(Dumas et al., 2021)	21
Table 2.2 Mechanical properties of AISI 4140 (Han et al., 2024) and 316L SS	(Aridhi et
al., 2022)	22
Table 2.3 Johnson cook parameters of AISI 4140 (Han et al., 2024)	22
Table 2.4 Thermal properties of 316L (Aridhi et al., 2022) and AISI 4140 (I	lan et al.,
2024)	24
Table 2.5 Micro hardness measurements of AISI 4140 and 316L SS alloys	27
Table 2.6 Stress relief annealing conditions of AISI 410 and 316L SS	28
Table 2.7 Machining conditions of inserts according to the manufacturer	29
Table 2.8 Nomenclature of tool DNMG 150608 PF 4315	29
Table 2.9 Machining conditions of AISI 4140 and 316L according to (Aridhi et	al., 2022)
and (Han et al., 2024)	30
Table 2.10 New machining conditions of machining AISI4140 and 316L SS	31
Table 2.11 Parameters of measuring residual stresses using XRD method	32
Table 3.1 Measured tool geometry of DNMG 150608 PF 4315 and DNMG 15060	8 QM 235
	34
Table 3.2 Machining forces of AISI 4140 and 316L SS	35
Table 3.3 Geometrical surface state of samples measured by Alicona micros	cope and
simulated by mountain maps software	36
Table 3.4 Average tool wear measurements of inserts	37
Table 3.5 Experiment machining forces and numerical machining forces comp	
AISI 4140 cutting forces and penetration forces	39
Table 3.6 Experiment machining forces and numerical machining forces comp	arison for
316L SS cutting force and penetration force	40
Table 3.7 Comparison of residual stresses of experimental and numerical of su	rface45
Table 3.8 Residual stresses of peaks and valleys of groves	46
Table 3.9 Theoretical, experimental and numerical chip correlation for 316L S	S49

Table 3.10 Theoretical, experimental and numerical chip correlation for AISI 4140 .	50
Table 4.1 Pits characterization	59
Table 5.1 Comparison of microhardness measurements of AISI 4140	63
Table 5.2 Microhardness measurements of 316L SS	65

Nomenclature

Abbreviations & acronyms

AD Affected depth

ADH Adhesion

ANG Insert Angle

CTA Cutting tool angle

CLA Clearance angle

EDG Edge length

EQ Equivalent

ESR Edge sharpness radius

FEA Finite element analysis

HFL Heat flux

KPR Tool led angle

MAX Maximum

MEAN Mean

MIN Minimum

NUM Numerical

PH Precipitation hardened

SS Stainless Steel

TOT Total

REP Insert tip radius

RPM Rounds per minute

XRD X ray diffraction

Other symbols

a_p Depth of cut

- b Basquin parameter
- A Yield stress at reference conditions
- A₃ Heat partition coefficient between tool and workpiece
- B Hardening modulus
- C Strain rate sensitivity coefficient
- D Diameter
- f Feed
- F Force
- F_x Feed force
- F_y Cutting force
- F_z Penetration force
- G Gain
- h Uncut chip thickness
- K_t Stress concentration factor
- K_f Fatigue strength reduction ration
- L Cutoff length
- N Number of cycles
- n Strain hardening exponent
- m Thermal softening exponent
- q Notch sensitivity factor
- Ra Arithmetic roughness
- Rz Average maximum heigh
- S Cut section
- T Temperature
- T_m Melting temperature
- T_o Temperature at the reference
- V_c Cutting velocity

- V_s Sliding velocity
- Vb Flank wear
- Z Surface topography
- Zp Peak of the cut off length
- Zv Valley of the cut off length
- $\alpha\text{-Vb}$ Relief angle
 - $\sigma \qquad Stress$
- σ_{11} Tangential pressure
- σ_{22} Normal pressure
- $\Delta\sigma$ Stress range
- ω Stress step
- μ Coefficient of friction
- λ Wavelength

Chapter 1

Introduction and Literature review

1.1. Machining

Machining is a subtractive manufacturing technique that removes material from a substrate to achieve the desired geometry and surface finish. Various types of traditional machining operations include turning, milling, drilling, and grinding. What sets machining apart from other manufacturing technologies is its ability to attain extreme tolerance levels and high-quality surface finishes, which are often unattainable through methods such as casting, forging, or additive manufacturing. Precision machining is particularly crucial in several industries, including aeronautical, nuclear, biomedical, and high-performance automotive components. Unlike other manufacturing techniques, such as casting or forming, the parameters governing machining do not depend on the melting point or ductility of the material. This technique demonstrates versatility in the range of materials it can accommodate, including metals, plastics and polymers, ceramics, and composites.

Additive manufacturing techniques can produce intricate shapes. Further machining is necessary to produce the desired surface or geometry. While additive manufacturing is poised to be the future of production, machining remains vital for achieving crisp corners and internal features such as threads and bores. Additional machining is necessary to attain precise fits between two components. Diverse types of cutting tools are available to achieve complex forms and geometries. Machining is a cost-effective method for small batch production and prototyping compared to other manufacturing techniques such as casting or injection molding. Although such components or prototypes are produced, machining is necessary to attain the desired surfaces. Contemporary CNC machines are swift and adaptable, facilitating prompt design modifications.

Machining tools traverse the workpiece on each round, removing material. Each revolution of the material eliminates the form of a chip. This results in a flat surface, yet on a microscopic level, it produces a grooved configuration characteristic of a machined surface.

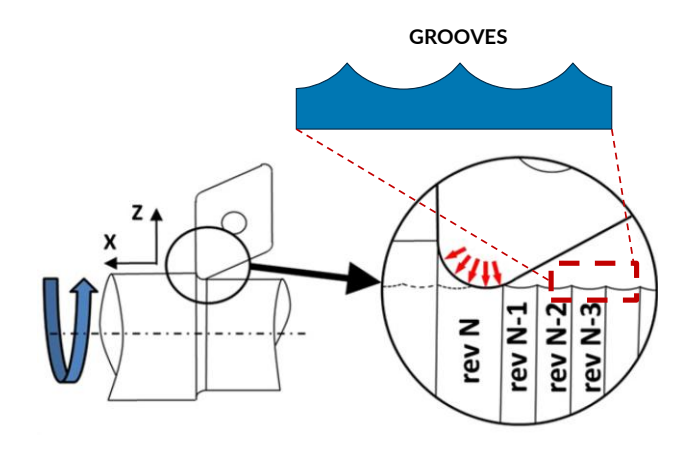


Figure 1.1 Groove formation during machining

This machining-induced surface integrity imparts distinct surface-related features, one of the primaries being fatigue-related qualities. In the next chapter, we will analyze in detail the surface integrity generated by manufacturing and its impact on fatigue.

1.2. Machining induced surfaces and fatigue life

Surface integrity relates to the surface topography resulting from the manufacturing process. The surface possesses distinct features compared to the bulk. It encompasses more than merely surface topography. It also encompasses hardness, microstructure, residual stress, flaws, and subsurface characteristics. These characteristics critically influence the functioning of the samples, including fatigue life, corrosion resistance, and tribological behavior of machined components. Each manufacturing sequence leads to specific surface integrity property mainly divided in to following (Field, 1971).

- Geometric parameters
- Mechanical parameters
- Metallurgical parameters

1.2.1. Geometrical parameters

Surface topography denotes the configuration or texture of a surface. It is meticulously guided by the manufacturing specifications. Machining is sensitive to cutting conditions, tooling, and lubrication. These surface finishes can result in crack initiation. Surface topography is quantified using several parameters, either two-dimensional (Ra, Rz, etc.) or three-dimensional (Sa, Ssk, etc.) (Arola & Williams, 2002). Numerous surface geometrical characteristics are referenced in literature; however, some of the more commonly utilized parameters are listed below.

Arithmetic average roughness (Ra)

Arithmetic roughness (Ra) is the absolute deviation of surface height from mean line over a specific length.

$$Ra = \frac{1}{L} \int_{0}^{L} |Z(x)| dx \tag{1.1}$$

Ra provides a comprehensive understanding of the surface texture, distinguishing between smooth and rough textures. A lower Ra value indicates a smoother surface. This number fails to accurately represent peaks or valleys.

Average maximum height of the profile (Rz)

Rz is known as average vertical distance between five highest peaks and deepest valleys over a specific length.

$$Rz = \frac{\sum_{i=0}^{5} Z_p - Z_v}{5} \tag{1.2}$$

Rz parameter is more sensitive to deep scratches than Ra parameters. This parameter is often used when there is a functionality.

(Chomienne et al., 2023) studied diverse surface topographies resulting from surface finishing technologies machining, belt finishing and ball burnishing. Figure 1.2 illustrates that various manufacturing procedures produce distinct surface topographies.

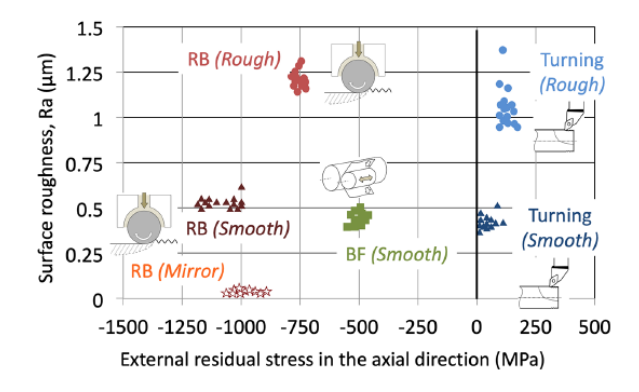


Figure 1.2 Surface integrity maps of the fatigue samples of 15-5ph (Chomienne et al., 2023)

This graphic demonstrates how various production processes provide distinct surface topographies. This illustrates a crucial point: even if the surface topography may be same, it might possess distinct mechanical characteristics.

1.2.2. Metallurgical parameters

Machining alters the metallurgical characteristics of the affected layers including microstructure, grain size, phase characteristics, and inclusions (Novovic et al., 2016). These parameters alter the fatigue characteristics of machined specimens. Numerous studies have demonstrated the evolution of microstructure in relation to industrial processes such as Turing grinding induces systematic microstructural alterations, including dynamic recrystallisation, which occurs during the turning process, resulting in the formation of a white layer on 15-5PH martensitic stainless steel (Mondelin et al., 2014).

(Dumas et al., 2021) examined the surface integrity resulting from the turning of 316L stainless steel. Three impacted depths have been designated as AD_0 , AD_1 , and AD_2 . AD_0 refers to the microstructure characterized by near-surface regions consisting of submicrometric grains approximately 1 μ m in size. AD_1 denotes the microstructure typified by significantly deformed grains exhibiting a high density of slip bands, with a depth of around 40 μ m. AD_2 is the entire impacted depth beneath which no additional slip bands exist, approximately 80 μ m. The affected depths vary with the fillet angle of machining. The hardness of the machined layer varies with the depth of the effect, grain orientation, and hardness.

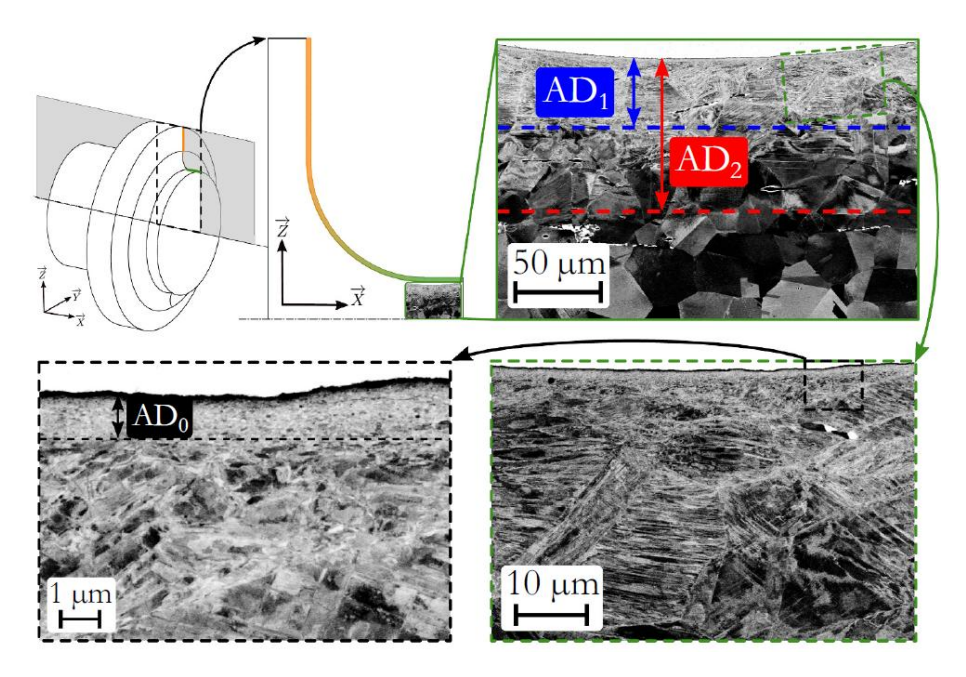


Figure 1.3 Turning-induced microstructure gradient beneath the surface in the case of longitudinal turning assessed by SEM (Dumas et al., 2021)

(Samant & Maity, n.d.) investigated the white layer formed during the hard turning of AISI 4140. These white layers are hard and brittle, comprising tensile residual stresses.

White layers are primarily created through three distinct mechanisms: plastic flow, rapid heating and quenching, and surface reaction with the environment. Three primary parameters found that influence the thickness of the white coating are cutting speed, flank wear, and depth of cut. The microstructure of affected layers is contingent upon manufacturing properties. In machining, the impacted layers are contingent upon machining parameters, such as the depth of cut. On flat surfaces, the depth of cut is reduced, and the feed rate is minimal. These machining parameters alter the impacted layers. Surface finishing procedures, such as belt finishing and roller burnishing, modify the microstructure of the resulting surface. These manufacturing procedures modify the impacted layers acquired.

1.2.3. Mechanical parameters

Manufacturing procedures modify the mechanical properties of the surface, including residual stress, microhardness etc. (Jawahir et al., 2011) investigated residual stresses caused by machining, specifically focusing on machining-induced residual stresses in multiple 100 µm. (Dumas et al., 2021) investigated microhardness resulting from the machining of fillets. Studies indicate that microhardness diminishes with increasing depth along the machined profile. (Chomienne et al., 2023) investigated the residual stresses induced by machining and surface finishing procedures, namely ball burnishing and belt finishing processes. Research indicates that turning and ball burnishing create compressive residual stresses, whereas rough turning produces compressive residual stresses on machined specimens. The same study indicates that rough turning generates tensile residual stresses on the surface, but smooth turning results in lower tensile stresses on the surface of 15-5 PH martensitic stainless steel.

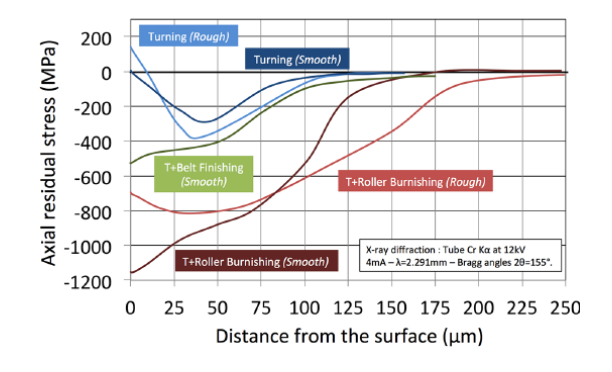


Figure 1.4 Average residual stress profiles obtained for each manufacturing sequence for 15-5 PH (Chomienne et al., 2023)

As stated, manufacturing technologies with varying parameters produce surfaces with distinct surface integrity characteristics (surface topographies, metallurgical properties, mechanical properties). The interplay of surface integrity factors alters fatigue strength.

This complicates the prediction of fatigue life effects. The research conducted by (Chomienne et al., 2023) indicates that the thickness of the compressive layer is a primary factor influencing the fatigue strength of 15-5 PH, with fatigue strength increasing due to dynamic recrystallisation. Surface roughness is a secondary determinant of fatigue strength. Fatigue strength is enhanced by a combination of minimal surface roughness and elevated compressive strength. This can be clearly seen from the results of the study mentioned in Figure 1.5.

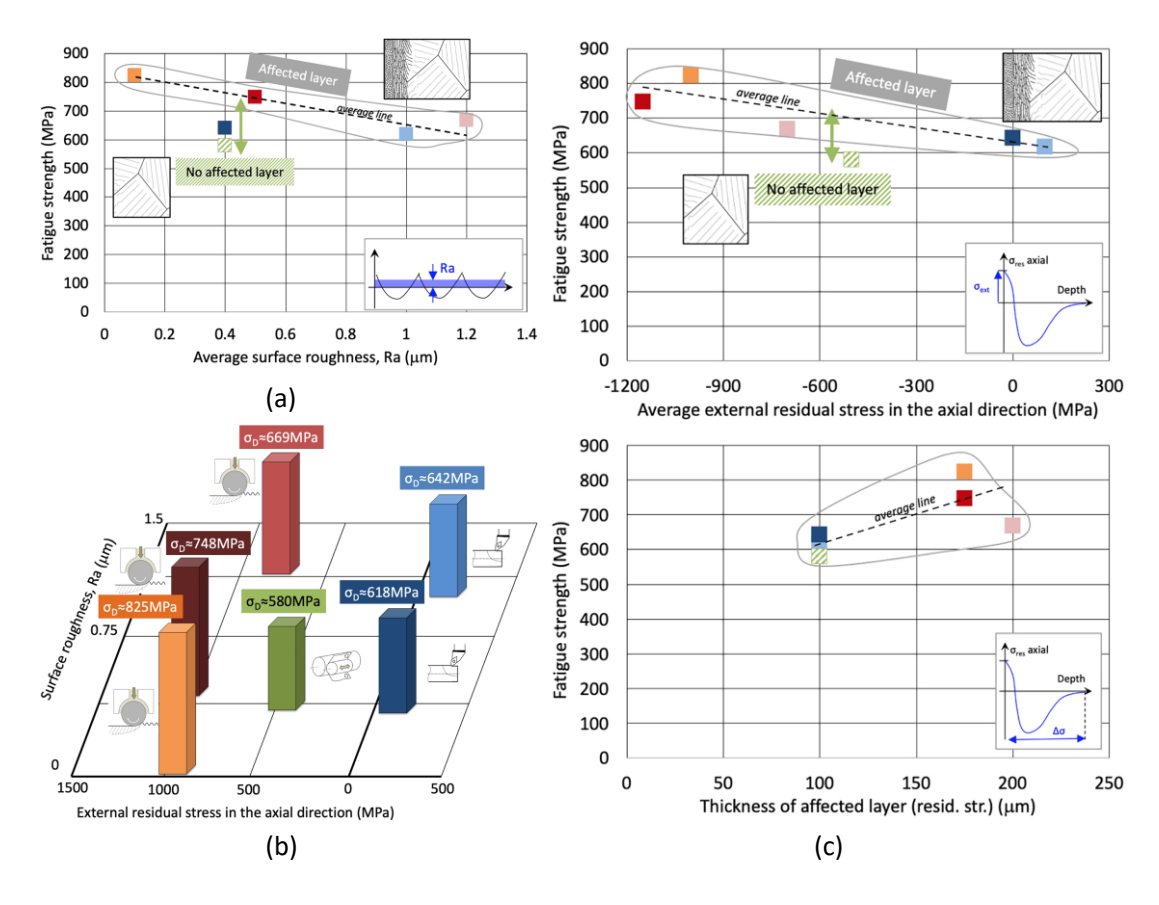


Figure 1.5 a) Surface integrity maps of the fatigue sample according to study conducted by b) Correlation between fatigue strength and surface roughness c) Correlation between fatigue strength and microstructure affected depth (Chomienne et al., 2023)

(Javidi et al., 2008) investigated the effects of machining on surface integrity and fatigue life. They attempt to correlate feed rate and nose radius effects, which are known to have a significant impact on the surface integrity of 34CrNiMo6 material. This investigation revealed a mechanically influenced layer of 3-4 µm after machining, no substantial

harness variation, and surface roughness at the same feed rate decreases with a small nose radius. Residual stresses tend to be more compressive as feed rate increases. It has been shown that feed rate and nose radius are important variables when managing residual stresses. Furthermore, increasing compressive residual stresses increases fatigue strength. (Berry et al., 2022) investigated milling-induced residual stresses on Aluminum 7075 and their influence on fatigue life. The testing includes a layer removal process to determine residual stress, followed by a three-point bending fatigue test. According to the study, increasing the feed while decreasing the cutting speed increases compressive residual stress at the material's surface. The fatigue testing results show that increasing compressive stress enhances fatigue life, with different impacts on long and short fracture propagation.

(Gerstenmeyer et al., 2018) investigated the effect of complimentary machining on fatigue strength of AISI 4140. According to studies, complimentary machining and grain refinement of AISI 4140 reduce the roughness of machined samples and convert residual stresses to compressive residual stresses. The study found that adding 5% to the likelihood of fracture increased fatigue strength by up to 63%.(Meyer et al., 2020)investigated the effect of residual stress depth distribution on the lifecycle behavior of AISI 4140. The experimental results reveal that the higher the residual stress penetration depth, the longer the longevity. Furthermore, deep rolling enhanced residual stress penetration depth, which improved longevity. This longer longevity can be explained by increased residual stress stability.

(Jouini et al., 2020) studied the influence of surface integrity on fatigue life of bearing rings by precision hard turning and grinding. The study shows that precision hard turning can achieve low surface roughness than by grinding. Both processes introduce microstructural changes. At subsurface, precision hard turning induces subsurface compressive and maximum residual stresses at $10\text{--}50~\mu\text{m}$ depth, corresponding to the transition zone formed after a thin white layer (<1 μ m). Grinding induces tensile residual stresses from 15 μ m depth, corresponding to the bulk material. The ring specimens machined by precision hard turning have fatigue life four times higher than those machined by grinding. This enhancement of rolling contact fatigue life is due to the low roughness reached and to the subsurface compressive residual stresses at shallow depth before rolling contact fatigue test.

1.3. Modelling of residual stresses induced by machining

The previous chapter addressed how global surface integrity parameters influence the fatigue strength of machined components. However, in the context of high cycle fatigue, cracks originate from microscale surface flaws. The surface integrity qualities must be evaluated microscopically. Certain microscopic surface integrity metrics cannot be empirically measured. This elucidates the necessity of modelling. This chapter discusses the modelling of machining operations to capture the mechanical characteristics of surface integrity caused by machining.

Plenty of cutting models have been created in literature. 2D numerical cutting models facilitate a swift and comprehensible understanding of the cutting process. 2D numerical models produced by (Ulutan & Ozel, 2011) offer essential insights into the machining process. However, these models incorporate robust assumptions that significantly deviate from reality. Machining alters the surface integrity and residual stresses of the processed component. The final machining operation is mostly responsible for the residual stresses created in the machined component (Guo & Liu, 2002).

(Shet & Deng, 2003) has developed a 2D numerical Lagrangian cutting model for the orthogonal cutting operation; nevertheless, these models are much detached from reality due to stringent assumptions, such as the consideration of the cutting action as a 2D plane strain configuration. Several issues arise with the 2D Lagrange orthogonal cutting model, as the 2D representation deviates significantly from reality. Significant mesh distortion was observed at the edge sharpness radius of Lagrange meshed solids. This phenomenon has been explained by (Ee et al., 2005). The inadequate friction between the Lagrange solid and the tool in the 2D orthogonal model is elucidated by (Liu & Guo, 2000). (Nasr et al., 2007) attempted to address the a forementioned problems with the 2D arbitrary Lagrange model; however, the explicit time integration procedures employed in these models complicate the calculation of relaxation time, which is essential for accurately representing residual stresses.

Based on the comprehension of 2D cutting models, research aims to simulate the residual stresses generated by machining, incorporating 3D cutting models throughout numerous revolutions. (Mondelin et al., 2012) has demonstrated that cutting tools alter residual stresses, which in turn affects the resolution achieved by prior measurements, necessitating multiple revolutions to attain steady-state residual stresses.

A different approach to modelling residual stresses has been put out by (Mondelin et al., 2012), which involves removing the chip formation by similar thermomechanical loadings. The issues brought on by the warped meshing parts can be resolved with this technique. Within the machining surface, these thermomechanical loadings move in a way that is consistent with the cutting velocity. It is simple to model the residual stresses brought on by the machining after the cooling phase has passed. Benefits of this residual stress prediction technique include the ability to simulate residual stresses for several revolutions and the lack of significantly distorted meshes.

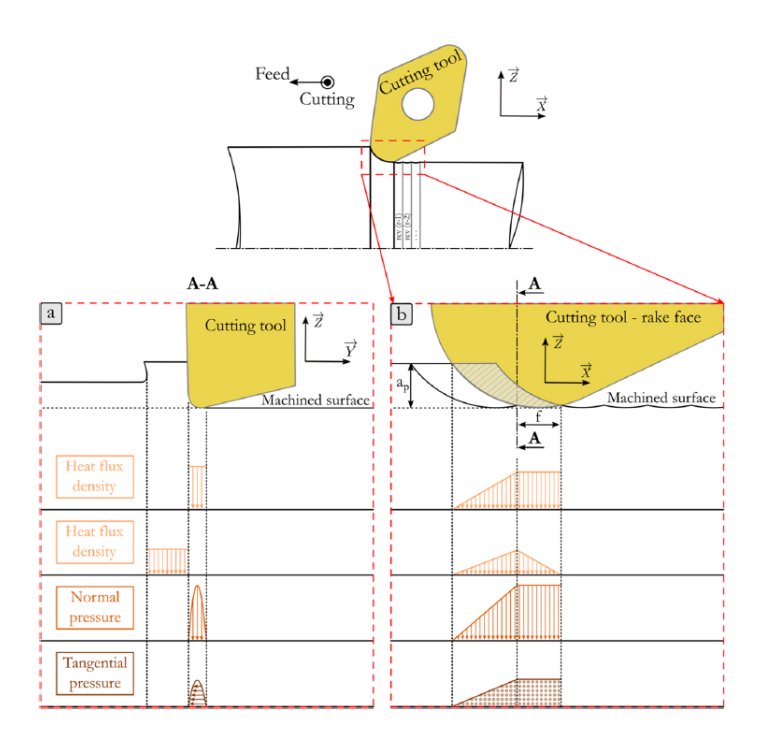


Figure 1.6 Simplified thermos-mechanical loadings mentioned in the(Mondelin et al., 2012)

Thermal mechanical loadings have basic loading shapes (homogeneous, parabolic, or linear), as seen in the figure model by (Mondelin et al., 2012). These loading shapes depend on the region (primary or tertiary shear zone) and the sections. As stated in the section, friction testing and orthogonal cutting tests are used to calibrate thermomechanical loadings. The flat surface was then subjected to these calibrated thermomechanical loads, which moved the cutting tool on the sample in relation to the sample. After that, thermomechanical loadings are applied for several revolutions until residual stresses in the steady state are achieved. The numerical residual stresses and steady state residual stresses were then contrasted.

This approach does have certain limitations, though. A flat surface was subjected to the thermomechanical loadings described in the model which is not quite accurate. As shown

in Figure 1.7 tool material interaction in machining is much more accurate in shape of cylindrical groove. Additionally, thermomechanical loadings can be better quantified and distributed. 3D numerical methods based on a two-scale approach based on advanced equivalent thermomechanical loadings have emerged in response to the shortcomings of earlier research. The two-scale approach's flow chart is provided in Figure 1.8 (Dumas, Fabre, et al., 2021a).

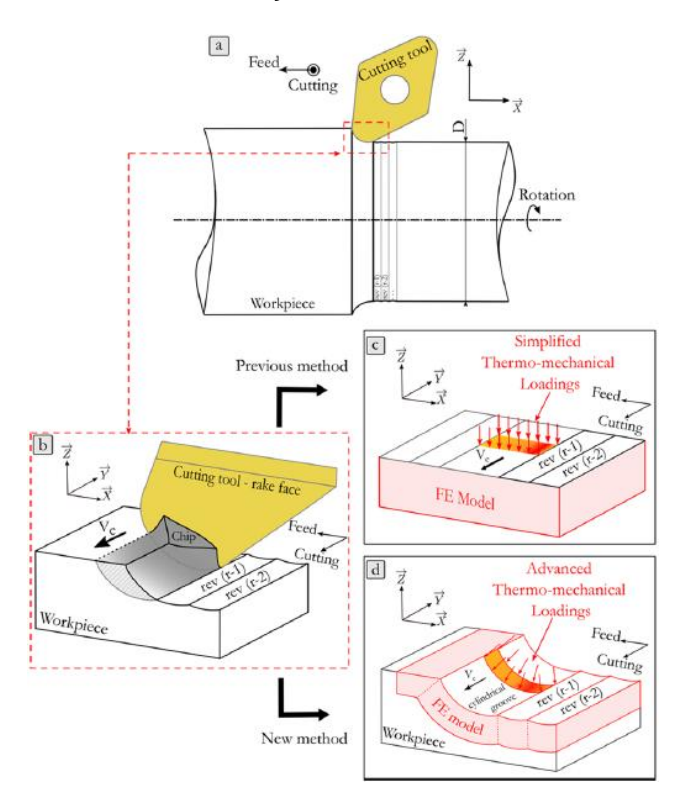


Figure 1.7 Principle of the residual stress modelling based on a two-scale approach. a) longitudinal turning operation, b) zoom on the chip formation zone, c) turning operation modelling based on equivalent thermo-mechanical loadings (Mondelin et al., 2012), d) turning operation modelling based on new advanced equivalent thermo-mechanical loadings (Aridhi et al., 2022)

The model begins extracting experiment cutting forces which are cutting force, penetration force and feed force. Then modeling begin by constructing a cut section S(i), which shows how the tool and material interact with the workpiece, as shown in the flow chart below. This cut segment has a local uncut chip thickness of h(i) and is separated into many 2D elementary orthogonal parts. As seen in the flow chart, a 2D numerical model is run in Abaqus using an Arbitrary Lagragian Eularian formulation for each section S(i). The extraction path was used to derive thermomechanical loadings for these 2D orthogonal models. Along the extraction path, the 2D model's heat flux, tangential pressure, and normal pressure are extracted. With combining and interpolation, this model successfully models the 3D load of heat flow, normal pressure, and tangential

pressure for a chosen S(i). The geometry of the thermo mechanical loadings is important because 2D numerical simulations are unable to adequately assess them.

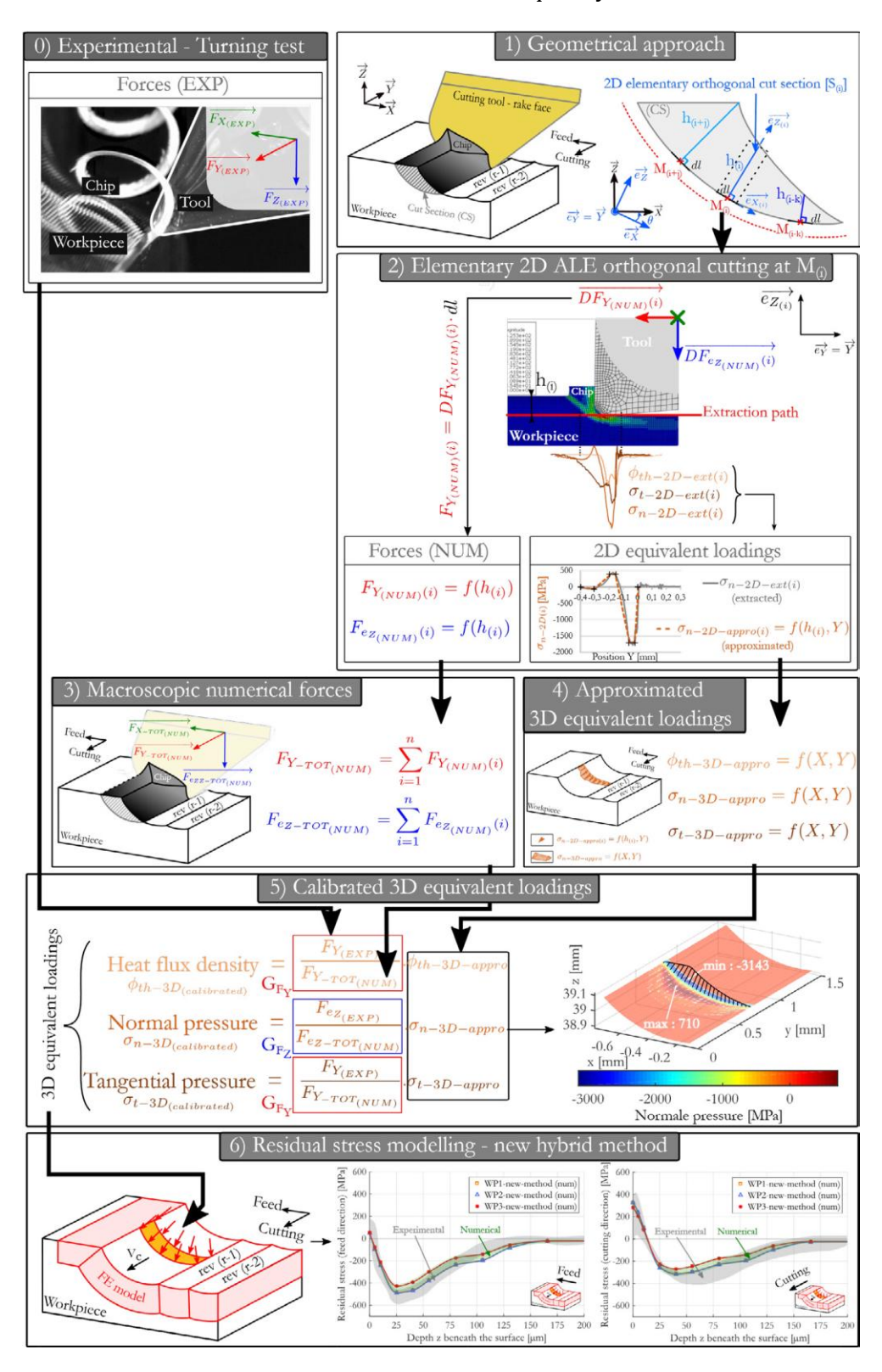


Figure 1.8 Flowchart of the new 3D hybrid methodology (Dumas, Fabre, et al., 2021b)

Modelled 3D thermomechanical loading may not always be precise. These loadings must be validated using experimental cutting forces. Thermomechanical loadings are calibrated by Gain. The equation for calculating gain is shown below.

$$G_{FY} = \frac{F_{y (EXP)}}{F_{Y - TOT (NUM)}} \tag{1.3}$$

$$G_{FZ} = \frac{F_{Z (EXP)}}{F_{Z - TOT (NUM)}} \tag{1.4}$$

 G_{FY} is used for the calibration of heat flux and tangential pressure and G_{FZ} is used for the calibration of normal pressure. Then 3D modeled cylindrical grove is then subjected to calibrated thermomechanical loadings for several revolutions to recover residual stress using the implicit formulation-based finite element program SYSWELD.

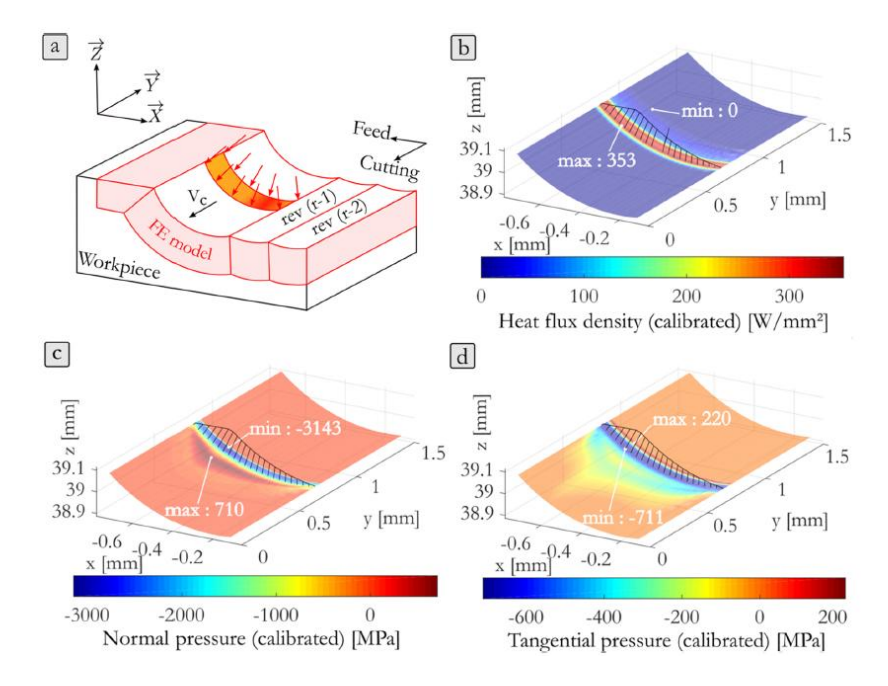


Figure 1.9 Final 3D equivalent thermo-mechanical loadings description with physical shapes and corrected intensities. a) finite element model, b) heat flux density, c) normal pressure d) tangential pressure (Dumas et al., 2021a)

Simulated and calibrated thermomechanical loadings are applied to the grooves at the cutting speed. However, the application of thermomechanical loadings in a single groove and subsequent simulation proved insufficient for the stabilization and accuracy of residual stress modelling. However, these fields must transition from one groove to another. The theory of field transmission theory is well explained in (Kermouche et al., 2009).

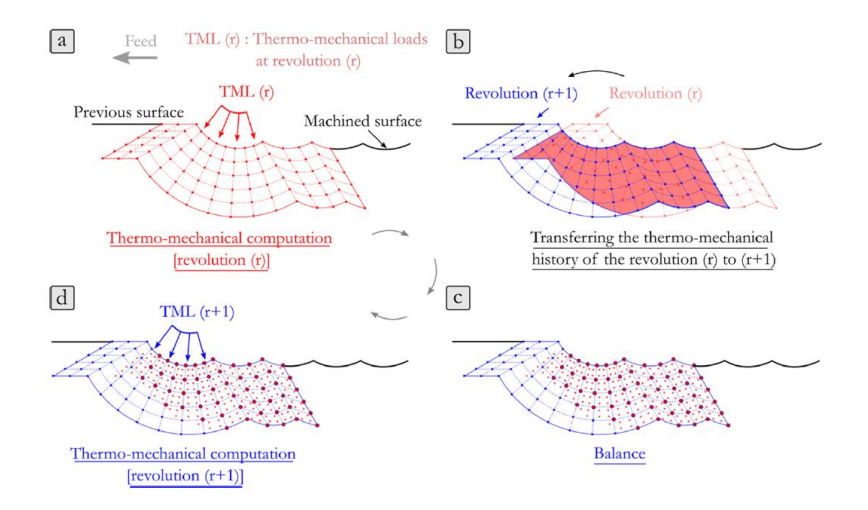


Figure 1.10 Field transfer procedure used for the modelling of several cutting tool passages

Few investigations have been conducted to examine the accuracy of this model using various materials. The validity of the model was verified through testing in studies conducted for 15-5 PH (Dumas et al., 2021a), AISI 4140 (Han et al., 2024), and 316L SS (Aridhi et al., 2022).

1.3.1. Modelling of Friction coefficient

(Mondelin et al., 2012) conducted friction tests to investigate how the heat partition coefficient and friction coefficient vary with sliding velocity and attempted to construct a friction model using tribological testing. Tribological experiments were performed on 15-5 PH material using a pin of a comparable material and a cutting tool made of cemented carbide. Investigate corelate with sliding speed, cutting speed, and machining operation. The model generated by the study is shown below.

For coefficient of friction,

For $10 \text{ m min}^{-1} < V_s < 300 \text{ m min}^{-1}$

$$\mu_{adh} = 2.12 V_s^{-0.45} \tag{1.5}$$

For $V_s > 300 \text{ m min}^{-1} \mu_{adh} = 0.15$

Heat partition coefficient for the study is defined as below.

$$A_3 = \frac{\phi_{pin}}{\phi_{tot}} \tag{1.6}$$

Model developed for this heat partition coefficient is given below.

For $V_s > 300 \text{ m min}^{-1}$, $A_3 = 25\%$

For $50 \text{ m min}^{-1} < V_s < 300 \text{ m min}^{-1}$,

$$A_3 = 230V_s^{-0.63} (1.7)$$

For $V_s < 50 \text{ m min}^{-1}$, $A_3 = 5\%$

The two-scale method of modelling residual stress is an intriguing approach that focusses on surface residual stress caused by machining at a microscale level. One of the most intriguing findings is the presence of a residual stress gradient that aligns with the contour of the groove. The XRD technique measures the mesoscopic average of surface residual stresses. The XRD technique averages residual stresses over the surface, rendering it unable to accurately identifying surface residual stresses, which may be achieved by a two-scale modelling approach (Dumas, Fabre, et al., 2021a).

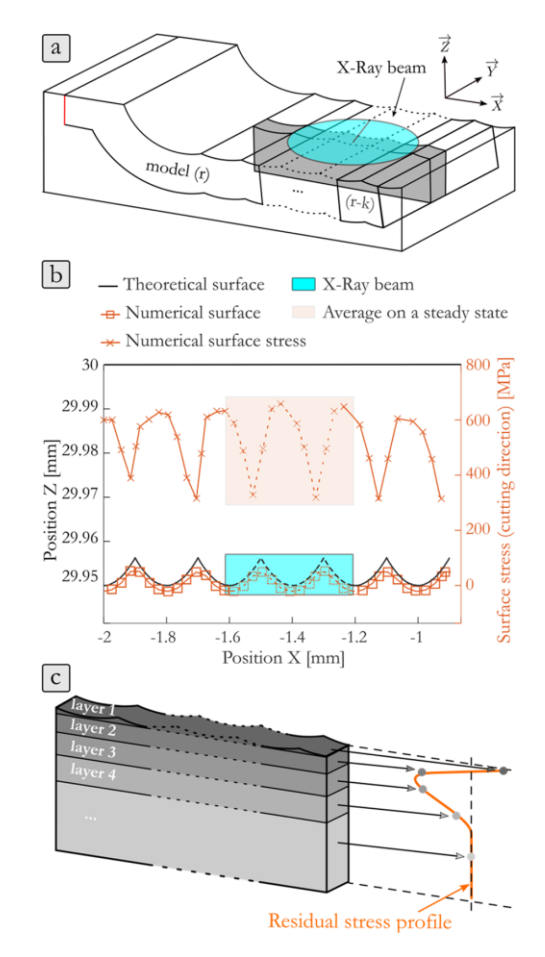


Figure 1.11 Numerical residual stress profiles building methodology, a) model overlapping of successive revolutions, b) surface residual stress average on a stabilized zone, c) in-depth average layer by layer for residual stress profile building (Dumas, Fabre, et al., 2021a)

This contradicts the fatigue-related findings mentioned in the preceding chapter. It was assumed that the machined surface is smooth and that its mechanical characteristics are homogeneous throughout. The fatigue characteristics of the machined components must

be studied, taking these variables into account. The subsequent chapter will address the principles of fatigue.

1.4. Fatigue life

Fatigue failure is a progressive phenomenon resulting from the repeated application of loads. It is among the most prevalent metallic failures. It is caused by metal being subjected to fluctuations in stress and strains. Prolonged repetitive loading results in cumulative damage to the component and an abrupt failure of the metal component(Santecchia et al., 2016). Fatigue failure comprises two stages: crack initiation and crack propagation. Crack initiation refers to the emergence of microcracks resulting from the accumulation of elevated stresses at a specific place, dislocations, and plastic deformation surrounding inhomogeneous regions near the surface. Crack growth results in irreversible damage to the mechanical component (Fajdiga & Sraml, 2009).

There are two fatigue regimes: low cycle fatigue and high cycle fatigue. When reparative loading cycles exceed 100,000, and more frequently, 10^6 or 10^7 cycles at high frequency and limited amplitude, high cycle fatigue results. In high cycle fatigue testing, the cycle to failure rises as loading amplitude falls. The applied high cycle fatigue loading is less than the yield strength. Given that the test material is in an elastic zone. Due to the restricted heat dissipation offered by straining, high frequency can be employed for high cycle fatigue testing without self-heating. Given that fatigue testing is currently conducted with frequencies between 100 Hz and 300 Hz. Non-metallic inclusions, small flaw and inhomogeneities of mechanical components are most life to initiate the cracks in high cycle fatigue (Nadot, 2022), (Zerbst et al., 2019).

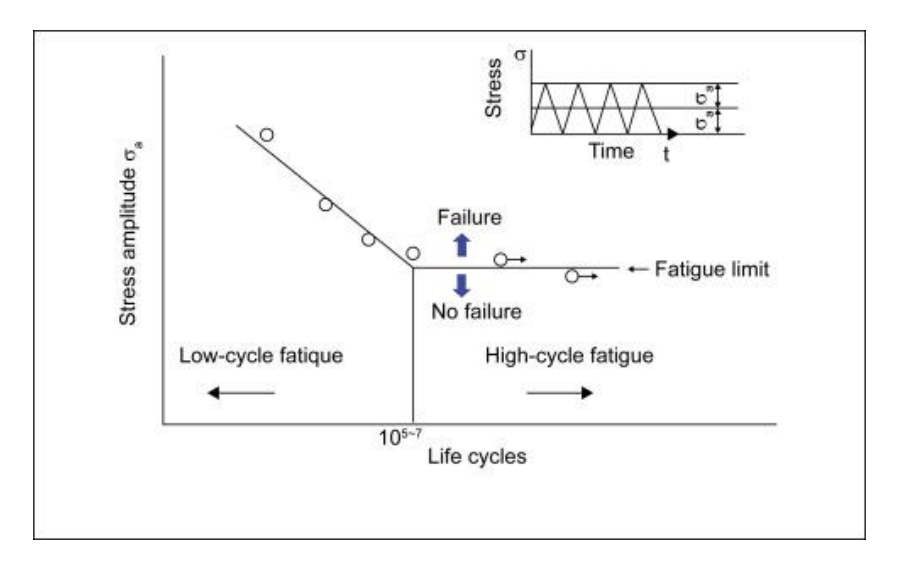


Figure 1.12 Wohler curve (Enomoto, 2022)

(Limodin & Verreman, 2006) examined the enhancement of fatigue strength in 4140 steel using gas nitriding and discovered that gas-nitrided 4140 steel is more prone to crack initiation from surface or internal fisheye cracking. Research indicates that sufficient nitriding depth enhances internal processes, hence improving fatigue strength. (Januário Cordeiro Gomes et al., 2015) examined the effect of surface roughness on ultrahigh cycle fatigue of AISI 4140 and determined that surface roughness had minimal impact on the samples, whereas surface compressive residual stresses significantly affected the fatigue life of AISI 4140.

1.4.1. Nomenclature for HCF

Mean stress applied from averaging the maximum and minimum stress applied.

$$\sigma_{mean} = \frac{(\sigma_{max} + \sigma_{min})}{2} \tag{1.8}$$

Stress range is calculated using equation below.

$$\Delta \sigma = (\sigma_{max} - \sigma_{min}) \tag{1.9}$$

Stress amplitude represents half of the range of applied. Calculated using the equation below. Stress amplitude is a crucial parameter in the Wohler curve, which is plot stress amplitude against number of cycles to failure.

$$\sigma_a = \frac{\Delta \sigma}{2} \tag{1.10}$$

Stress ratio is defined as the ratio of minimum to maximum cyclic stress. Calculation of stress ratio is given below.

$$R = \frac{\sigma_{min}}{\sigma_{max}} \tag{1.11}$$

Common values used in loadings,

Value	Conditions
R = -1	Fully reversed loading condition, consists of tensile and compressive stress
R = 0	Zero to tension loading which is minimum stress is zero but positive maximum stress
0 < R < 1	Repetitive tensile loading
R > 1	Repetitive compressive loading

Table 1.1 Stress ratio common values and their interpretations

Certain materials have a discernible limit for high cycle fatigue on the Wohler curve. Certain materials exhibit a reduction in stress amplitude as the number of cycles to failure increases, without evidence of infinite fatigue life.

A broad relation exists between the fatigue strength, known as the endurance limit, and the ultimate tensile strength for many steel alloys. This is elucidated by the endurance ratio. The endurance ratio is a dimensionless statistic that delineates the relationship between fatigue strength and ultimate tensile strength.

$$Endurence\ ratio = \frac{Fatigue\ stregnth}{Ultimate\ tensile\ stregnth} \tag{1.12}$$

The endurance ratio typically ranges from 0.35 to 0.6. The endurance ratio offers a rapid assessment of fatigue strength in relation to overall strength. Materials with a high endurance ratio have superior tensile strength when subjected to cyclic loading. However, these ratios fluctuate due to variables including steel type, surface finish, heat treatment, dimensions and shape, as well as notches or stress concentrations.

Real mechanical components having varied non-homogeneous geometries, surfaces read to the stress variation within the samples. These criteria need to always take into account while designing due to their effect on fatigue life. To assess the surface geometry of the samples, the stress concentration factor has been defined. The stress concentration factor is a dimensionless quantity that measures the extent to which local stress intensifies due to geometric discontinuities, such cavities, pores, or notches. The stress concentration factor is essential for predicting stress increases caused by geometric imperfections and for reducing the associated risks of stress concentration.

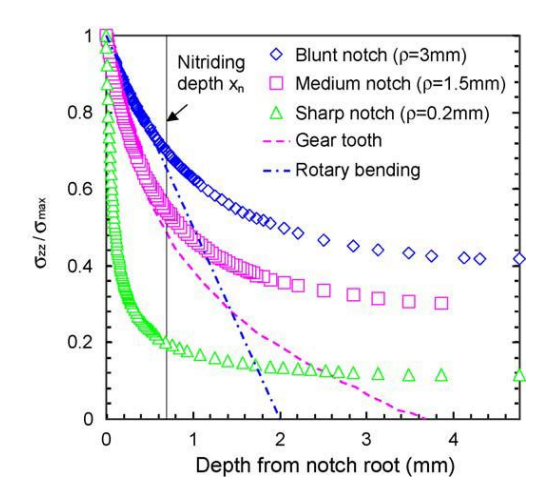


Figure 1.13 Stress gradient of the notched specimen (Limodin & Verreman, 2006)

Owing to the geometrical features of the geometry, the maximum linear-elastic principal stress gradually decreases along the bisector from the apex of the notch to the midsection of the specimen itself. If the net width of the sample is large enough, the above stress field tends to its nominal net value. At the tip of the notch instead the maximum principal stress reaches its maximum value, linear-elastic peak stress (Susmel, 2009).

$$K_{t,net} = \frac{\sigma_{ep}}{\sigma_{net}} \tag{1.13}$$

$$K_{t,gross} = \frac{\sigma_{ep}}{\sigma_{gross}} \tag{1.14}$$

Stress concentration factor previously mentioned may directly apply to fatigue calculations. Experiments have shown that fatigue strength reduction factor is different from the stress concentration factor. From microscopic point of view only steep elastic stress gradient is not only sufficient for shuttle dislocation and nucleating a crack. Experiments evidence has shown that fatigue stress reduction factor is less or equal to the stress concentration factor (Vernon & Mackin, 2001).

The fatigue strength reduction factor, K_f , is defined to assess the impact of notches on fatigue life. The fatigue strength reduction factor is delineated below.

$$K_f = (\frac{Fatigue\ stregnth\ of\ smooth\ specimen}{Fatigue\ stregnth\ of\ notched\ specimen}) \tag{1.15}$$

The specific notch stress concentration factor exceeds the fatigue reduction factor. The fatigue strength reduction factor K_f is a dimensionless quantity that is contingent upon the material properties. K_t is a dimensionless factor that is contingent upon geometry rather than material properties.

In this context, the fatigue notch sensitivity factor (q) is established to quantify the sensitivity of a particular notch (ASTM Special Technical Publication, 1949).

$$q = \frac{(K_f - 1)}{(K_t - 1)} \tag{1.16}$$

Notch sensitivity factor depends on the notch radius and materials ultimate tensile strength.

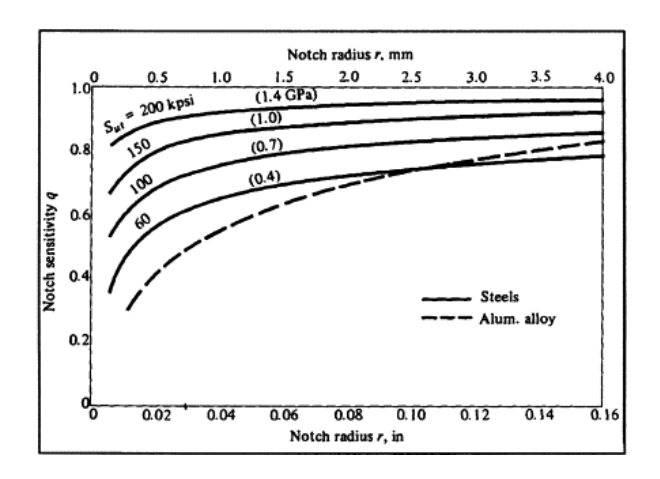


Figure 1.14 Notch sensitivity for various materials (Vernon & Mackin, 2001)

(Majzoobi & Daemi, 2010) studied the effect of notch geometry on fatigue life using notch sensitivity factor. Study compared 2 materials with 3 types of notches and stress concentration factor is calculated by numerical methods and fatigue stress reduction factor was determined by the experimentation. Results show that notch geometry has profound effect on the fatigue life of the materials. Higher the notch sensitivity lowers the fatigue life of the materials.

Low cycle fatigue refers to the failure of a component resulting from periodic cycles which excess of the endurance limit commonly known as between 10⁴ and 10⁵. Generally low cycle fatigue is shown with total strain vs number of cycles to failure (Parida, 2001). Inelastic deformation occurs in the samples due to elevated stress amplitude. Low cycle fatigue loadings have elevated stress amplitudes at low frequency. This inelastic deformation facilitates substantial heat dissipation. In low cycle fatigue, fatigue testing is conducted at low frequencies ranging from 1 to 5 Hz. Plastic deformation induces distinct slip bands on the surface, which facilitate both crack development and propagation. In such a damage mechanism, less dispersed data is observed.

1.4.2. Fatigue testing

Multiple techniques exist for assessing the endurance limit. The Locati method is a technique employed to ascertain the endurance limit more rapidly with few specimens (e.g 3 parts).

Principal of the Locati method is given below. The first part tested during specific number of cycles at specific stress amplitude($\sigma_{1,a}$). If sample does not occur failure, stress level increased by step (λ) and then sample runs for the same number of cycles (N). This periodic method is used until failure occurs. Then mean fatigue strength for N number of cycles have determined using following equation.

$$\sigma_{e,a} = \left(\frac{N_1}{N}\sigma_{1,a}^b + \frac{N_2}{N}\sigma_{2,a}^b + \frac{N_3}{N}\sigma_{3,a}^b\right)^{\frac{1}{b}}$$
(1.17)

 Σ _e is the equivalent fatigue strength for N number of cycles. N_i number of cycles at $\sigma_{i,a}$ stress amplitude and b is Basquin parameter. Initial stress amplitude of the following sample depends on the fatigue strength of the previous sample.

$$\sigma = \sigma_m - 2\omega \tag{1.18}$$

 σ_m corresponded to mean of the fatigue strength of the previous samples and it also corresponds to the fatigue strength of material for N number of cycles end of the process.

The Locati method is a rapid, efficient, and cost-effective technique for determining the fatigue limit of samples. Plotting the number of cycles to failure against stress amplitude can determine the endurance limit. The accuracy of the endurance limit is diminished due to the limited number of samples tested. The exclusion of cumulative load is not universally applicable (Beaumont et al., 2012).

1.5. Research gap and objectives

As noted in the literature review in chapter 1.2, research was conducted on the global residual stresses induced by machining and their impact on fatigue life. Two scale techniques to modelling residual stress were effective in capturing local residual stresses caused by machining. However, residual stresses created by machining on local scale and their influence on fatigue life are a unique subject that will be explored in this article.

Main objectives of this academic research are given below.

- Analyze crack initiation of fatigue samples manufactured by machining with and without residual stress
- Model residual stresses are induced by machining using two scale approach to model 3D residual stresses.

Chapter 2

Materials and Methods

2.1. Material properties

Materials were selected for this study were AISI 4140 and 316L materials.

AISI 4140 is a medium carbon, low allow steel with minimal Chromium and Molybdanium. These elements give the alloy the necessary strength, hardness, and wear resistance. This applies to all 41XX alloys (Smith, 1993). This metal is commonly utilized in the automotive sector for driving elements (steering components, cracked shafts), forged parts, bolted assemblies, and so on. Material has production features such as high machinability and intriguing fatigue behavior; however, it is frequently subjected to oxidation (Abd El Whaab, 2014).

316L SS is an austenitic stainless steel that is widely utilized in many industries. 316L SS is used in nuclear engineering structural materials, particularly primary cooland pipes and main cooland pipes in pressurized reactors, because to its characteristics. 316 L SS materials provide features such as improved weldability, reduced radiation sensitivity, and oxidation resistance (Hu et al., 2020). However, it has low heat conductivity and high ductility, which reduces the material's machinability (Philip & Chakraborty, 2022).

Composition of AISI 4140 and 316L SS materials given below.

Elements	С	Mn	Si	Ni	Mo	Cr	Cu	P	S	Fe
(wt,%)										
316L SS	0.018	1.276	0.444	10.168	2.062	16.764	0.368	-	0.27	Bal.
AISI 4140	0.443	0.805	0.308	0.253	0.198	1.15	0.020	0.021	0.010	Bal.

Table 2.1 Materials composition of AISI 4140 (Badaruddin et al., 2019) **and 316L SS** (Dumas et al., 2021)

Mechanical properties of materials AISI 4140 and 316L SS is given below.

Materials property (unit)	Temperature (C)	316L	AISI 4140
Density (Kg/m³)	20	8000	7844
	300	7890	-
	500	7800	-
	800	7660	-
	1000	-	7434
	1100	7510	-
Youngs modulus (MPa)	20	197000	212000
	200	184000	-
	400	168000	-
	600	151500	-
	400	168000	-
	800	128000	-
	900	108000	-
	1200	-	137530
Poisson ratio	-	0.3	0.287

Table 2.2 Mechanical properties of AISI 4140 (Han et al., 2024) **and 316L SS** (Aridhi et al., 2022)

The previously mentioned properties indicate that AISI 4140 material exhibits greater brittleness than the 316L alloy. The plasticity of AISI 4140 is characterized by Johnson-Cook parameters. Plasticity in 316L stainless steel was derived from its experimental behavior at low levels.

A (MPa)	B (MPa)	С	m	n	Tm (°C)	To (°C)	ε.0 (s ⁻¹)
598	768	0.0137	0.807	0.2093	25	1520	1

Table 2.3 Johnson cook parameters of AISI 4140 (Han et al., 2024)

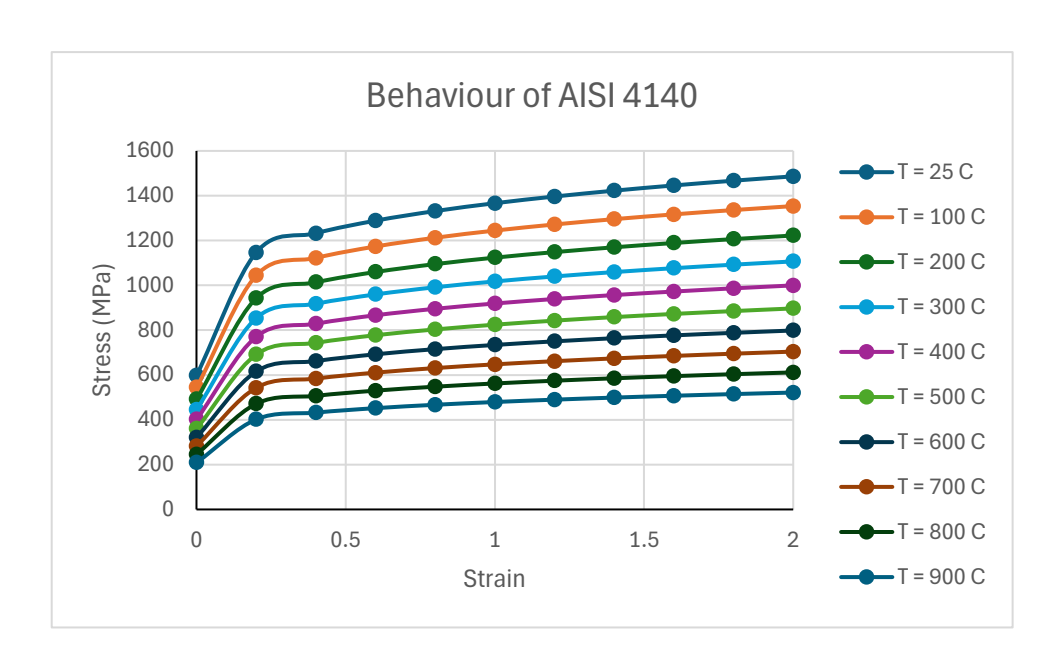


Figure 2.1 Behavior of AISI 4140 obtained from Johnson-Cook parameters

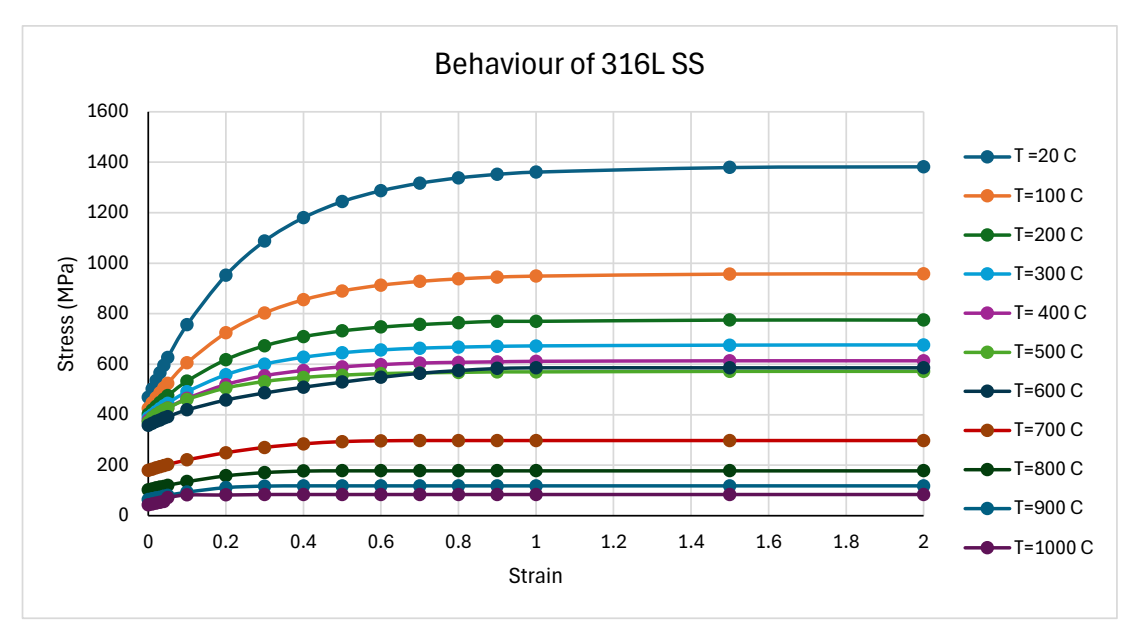


Figure 2.2 Behavior of 316L stainless steel (Lurdos, 2008)

Thermal parameters of AISI 4140 and 316L SS alloys are given below.

Material properties (unit)	Temperature (°C)	316L	AISI 4140
Thermal conductivity (W/m/C)	20	14	43.6
	200	-	41.7
	300	18	-
	400	-	38

500 600	21	-
500		
		32.8
300	24	-
1100	29	-
20	450	437
200	-	477
300	545	-
400	-	523
500	570	-
500	-	568
300	625	-
1100	670	-
)	0	0
20	0	0
22	0.0000159	-
23	-	0.0000112
200	0.000017	-
400	0.0000179	-
500	0.0000187	-
700	-	0.0000146
300	0.0000194	_
500	0.000011	
900	0.0000196	-
	1100 200 200 300 400 500 500 1100 0 20 22 23 200 400 500	1100 29 20 450 200 - 300 545 400 - 500 570 500 - 300 625 1100 670 0 0 20 0 22 0.0000159 23 - 200 0.000017 400 0.0000179 500 0.0000187

Table 2.4 Thermal properties of 316L (Aridhi et al., 2022) and AISI 4140 (Han et al., 2024)

2.2. Experiment Protocol of sample preparation

The experimental protocol was intended to ensure that samples surfaces have controlled grooves and residual stresses on the surfaces of the machined specimens. Stress relief heat treatments were conducted prior to machining to eliminate the material's thermal history, followed by additional stress relief annealing to ensure no residual stresses were produced in the machined samples. Then machining was conducted to get the geometry of the fatigue samples. During machining, cutting forces were measured and chip samples were collected for subsequent modelling.

After sequential machining and heat treatment, samples were measured for residual stresses using X-ray diffraction techniques. One set of samples was submitted to X-ray diffraction after machining, whereas the other set was treated to X-ray diffraction after both machining and heat treatment.

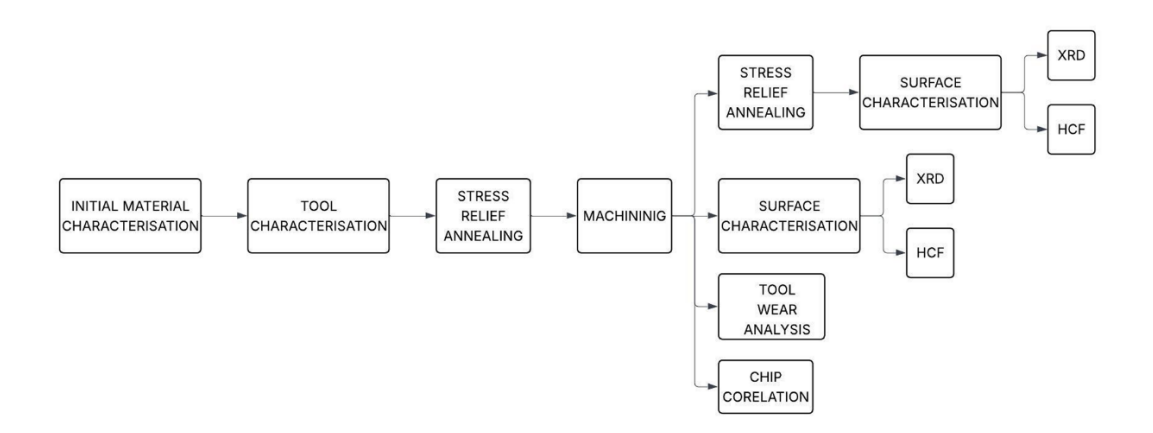


Figure 2.3 Experiment protocol for each material

Eight samples were produced for each material. Among these eight, four underwent machining followed by stress relief annealing, while four were exposed just to machining. From the two groups, one sample was subjected to XRD for residual stress analysis. Rest exposed to elevated cycle fatigue. A total of 16 samples were produced from two materials, with 4 analyzed by XRD and 12 submitted to high cycle fatigue testing.

2.3. Materials Characterization

Initially, materials were characterized using an optical microscope to check material microstructure, and microhardness tests were done to validate characteristics. This stage is necessary to validate the material that will be used in the study.

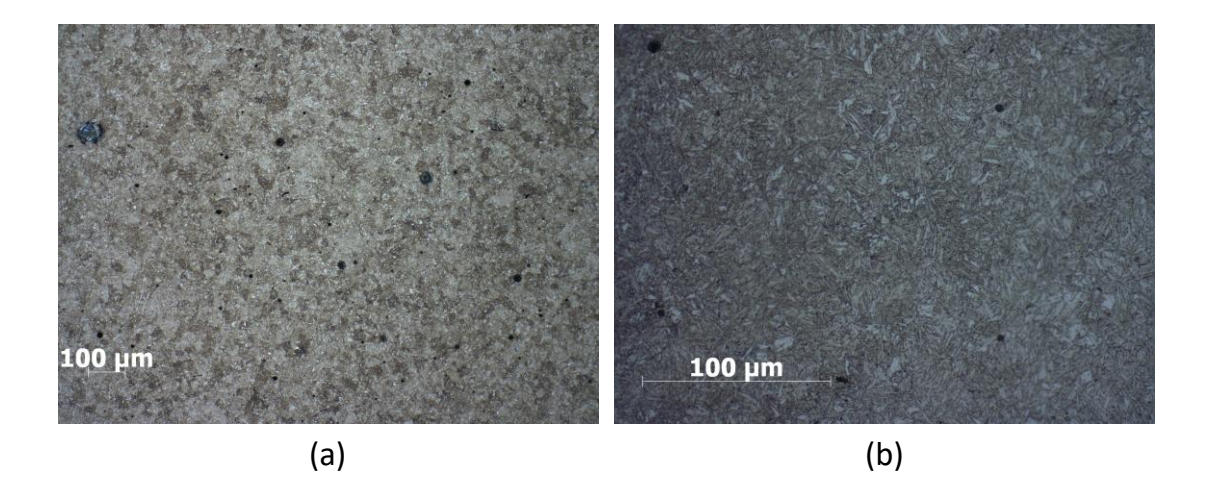


Figure 2.4 Microstructure observation of AISI 4140 a) 10x and b) 50x

From the microstructural observation it was noticed that AISI 4140 material has a ferritic microstructure shape of globular shape with inclusions which is coherent with the study conducted by (Ruiz De Eguilaz et al., 2010).

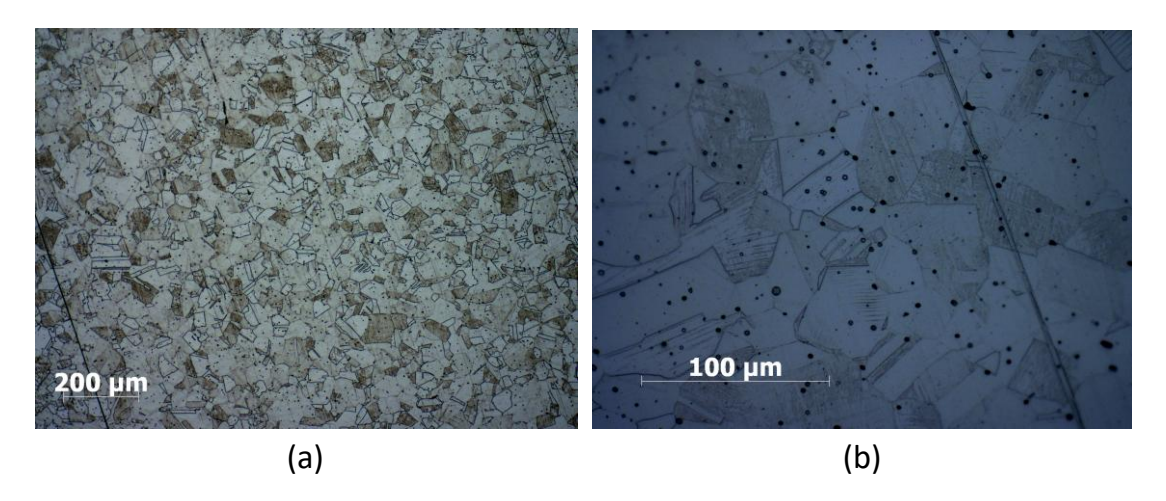


Figure 2.5 Microstructure observation of 316L a) 10x and b) 50x

Microstructural investigations indicate that 316L stainless steel possesses an austenitic microstructure including inclusions which is coherent with study conducted by (Dumas, Kermouche, et al., 2021).

Following the examination of the microstructure of both materials, microhardness tests were conducted to verify their properties. Objective of micro hardness test is to verify mechanical properties of materials and initial condition. Micro hardness measurements were carried out within the bulk several times and the within the bulk and average micro hardness were calculated and compared with literature to confirm material properties.

Material	Micro Hardness (0.3 HV)
AISI 4140	344.6
316L SS	250

Table 2.5 Micro hardness measurements of AISI 4140 and 316L SS alloys

2.4. Heat treatment

Heat treatment is used to relieve stress and eliminate residual strains without affecting the microstructure or properties. The stress release time and temperature of both materials vary depending on their composition.

There are three different temperature ranges for heat treating 316L. The sensitizing range is reported to be between 426 °C and 871 °C. Within this range, non-stabilized austenitic will undergo carbide precipitation, resulting in reduced corrosion resistance. Extra low carbon grades such as 316L or 304L fall inside this range since they will not be subjected to the sensitization that occurs during normal shop fabrication. They will become susceptible to intergranular corrosion following prolonged heating in the 537 °C to 593 °C range. 732 °C -954 °C is known as the stabilizing range. Within this range, some carbides can precipitate in a less hazardous manner. Materials other than 301, 302, 304, or 308 may exhibit some embrittlement. The annealing range is defined as temperatures ranging from 954°C to 1093°C.

(Elangeswaran et al., 2019) used post-heat treatment to investigate the fatigue behavior of 316L stainless steel produced by laser powder bed fusion. They discovered that stress-relieved samples do not produce substantial microstructure changes other than cellular coarsening. Sensitization is one of the most difficult heat treatments for 316L. (Chao et al., 2021) investigated the effects of post-processing heat treatment on the microstructure, residual stress, and mechanical properties of selective laser-melted 316L stainless steel. This study discovered that heating samples at 400°C for 4 hours did not modify the grain size, residual stresses were reduced by 23%, and mechanical characteristics remained mainly unchanged.

(A et al., 2020) investigated the influence of heat treatment on the predicted fatigue limit and Brinell hardness number. They tested stress relief at 500 °C, 600 °C, and 660 °C for 0.5 hours and discovered that stress relief over 600 °C reduces both fatigue limit and Brinell harness number. (Badaruddin et al., 2019) investigated the improvement of low cycle fatigue resistance in AISI 4140 steel with annealing treatment. Stress reduction

was administered at 815 °C for a duration of one hour. The furnace temperature was then reduced to 665 °C at a pace of 11 °C/min. (Menig et al., 2002) investigated the residual stress stability and alternating bending strength of AISI 4140 following shot peening and subsequent annealing. The results show that shot peening causes compressive residual stresses on the samples, while stress relief annealing at 300 °C - 500 °C maintained or improved residual stress stability. Stress treatment at 600 °C nearly recovered the residual strains, and fatigue strength increased by 22%. (Gür & Arda, 2003) investigated the influence of tube spinning and subsequent heat treatments on the strength, microstructure, and residual stress condition of AISI 4140. The results showed that the cold worked tubes had substantial tensile residual stresses, and stress relief annealing at 600 °C for 1 hour decreased the residual stresses from 300 MPa to less than 50 MPa. Considering the above-mentioned literature review stress relief conditions were confirmed.

Material	Temperature (°C)	Time (hours)
316L	450	5
AISI 4140	550	3

Table 2.6 Stress relief annealing conditions of AISI 410 and 316L SS

Stress relief heat treatment was performed inside an electric oven in a nitrogen atmosphere.

2.5. Tool Characterization

Machining tool and insert holders were chosen based on the geometry shape, availability, and machining conditions of the literature. Considering these parameters, machining inserts and tool holders were selected. For machining 316L, DNMG 150608 QM 235 was used, and for machining AISI 4140, DNMG 150608 PF 4315 was used. Tool holder PDNRR 2020 15A was chosen considering the geometry of sample and insert.

Insert	DNMG 150608 PF 4315	DNMG 150608 QM 235
V _c	230 m/min (230 - 290)	130 m/min (170 - 105)
a_p	0.3 mm (0.3-1.5)	1.5 mm (0.15 - 5)
f	0.1 mm/r (0.1 - 0.4)	0.25 mm/rev (0.1 - 0.4)
Coating	CVD TiCN+Al2O3+TiN	CVD TiCN+TiN

Table 2.7 Machining conditions of inserts according to the manufacturer

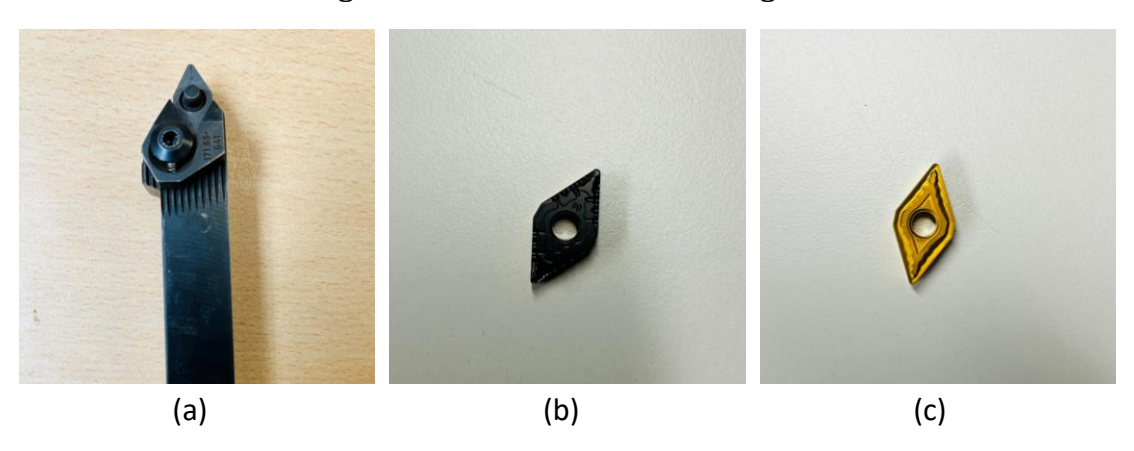


Figure 2.6 Insert holder PDNRR 2020 15A B) Insert DNMG 150608 PF 4315 C) DNMG 150608 QM 235

Insert nomenclature indicates specific characteristics of each insert. Here it is presented nomenclature and its meanings of insert DNMG 150608 PF 4315.

Terminology	Meaning	
D	Insert shape: Rhombic insert angle 55	
N	Relief Angle: 0	
М	Tolerance class: Medium	
G	Insert type: Hole and chip breaker, double sided	
15	Insert size	
06	Insert thickness: 6mm	
08	Nose radius: 0.8mm	
P	Chip breaker geometry: Steel machining applications	
F	Finishing grade chip breaker	
4315	Coating substrate: TiCN + Al2O3	

Table 2.8 Nomenclature of tool DNMG 150608 PF 4315

For DNMG 150608 QM 235, QM refers to the chip breaker geometry. Q refers to Light to medium machining and M refers to the medium cutting conditions.

The tool was characterized by using an Alicona Microscope. One insert was chosen for the roughing operation for all samples in the same material, and one insert was chosen for one sample in the semi-finishing and finishing operations. Each insert angle was measured three times for all inserts and averaged across all samples.

2.6. Machining

The fatigue samples are manufactured using machining. Samples were machined to provide regulated surface and residual stresses. Machining conditions were determined based on research conducted by (Han et al., 2024) and (Aridhi et al., 2022). The geometry of a fatigue testing sample is shown below.

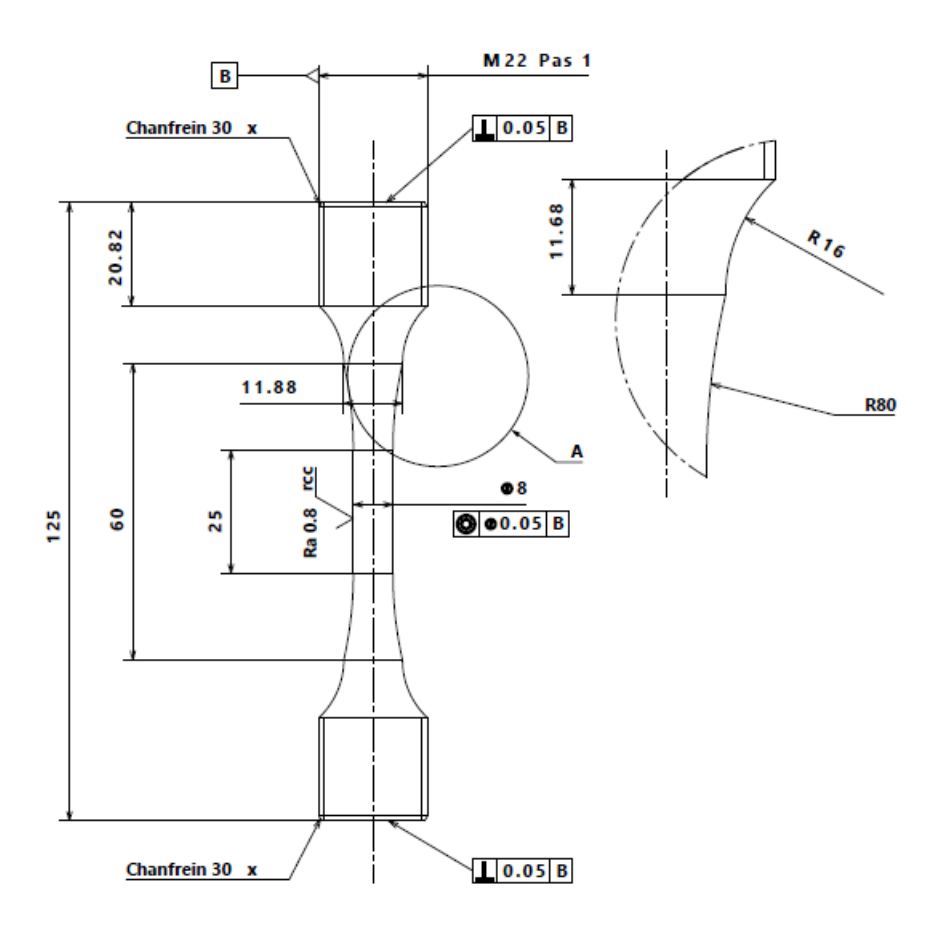


Figure 2.7 Engineering drawing of Fatigue simple

Materials	Cutting speed, V _c	Feed, f (mm/rev)	Depth of cut, a _p
	(m/min)		(mm)
316L SS	100	0.3	0.3
AISI 4140	200	0.1	0.2

Table 2.9 Machining conditions of AISI 4140 and 316L according to (Aridhi et al., 2022) **and** (Han et al., 2024)

Machining was conducted without lubrication. Machining was performed using CNC turning machine (CMZ TC25Y). During the machining cutting force signals were extracted using the Dynamometer (Kistler 9257A) and chips were extracted.

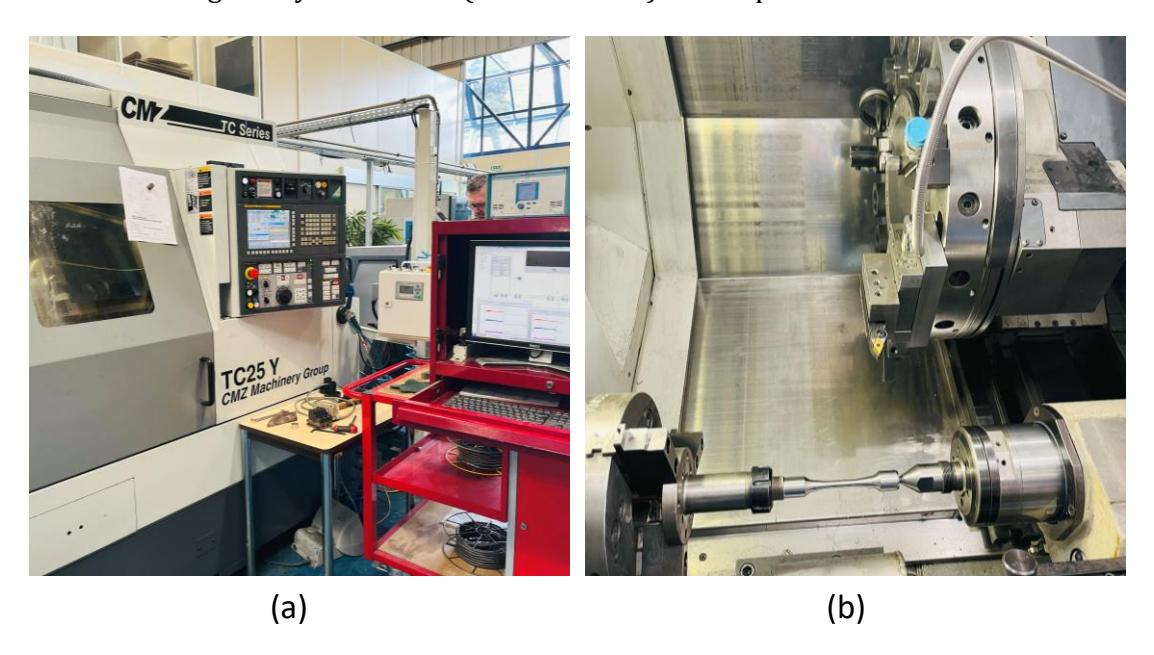


Figure 2.8 (a) Machine tool (b) Mounting of the sample to the lathe machine

Machine restrictions caused machining conditions to shift during the process. The machine tool can reach a maximum rpm of 4000. The maximum RPM at which a machine tool may operate is found using the equation below.

$$RPM = \frac{1000 * V_c}{\pi * D} \tag{2.1}$$

The engineering drawing for the sample has a minimum diameter of 8 mm. As a result, the highest cutting velocity achievable in the smallest diameter segment is 100.53 m/min. During the machining of 316L SS, vibration was noted. The machining conditions were modified to minimize vibration. The machining conditions were altered for the following reasons.

Material	Cutting speed, V _c	Feed, f (mm/rev)	Depth of cut, a _p
	(m/min)		(mm)
AISI 4140	100	0.2	0.3
316L SS	70	0.2	0.15

Table 2.10 New machining conditions of machining AISI4140 and 316L SS

Those machining conditions were used to machine all the samples.

2.7. X Ray Diffraction Measurement

Measurement of residual stresses are carried out using X ray diffraction method.

2.7.1. Bragg's law

Brags law describes the conditions for the constructive interface of X-rays scattered from distinct crystal planes. The crystal structure of metals is determined using Bragg's law. When the route difference between reflected waves equals an integer doubling of the wavelength, the waves reinforce each other, resulting in a diffraction peak.

$$n\lambda = 2dsin\theta \tag{2.2}$$

The Braggs law is used to calculate residual stress. Residual stress induces strain in the lattice, changing the interplanar distance and shifting the diffraction peak angle. By measuring this shift, residual strain is computed. Using residual stain, residual stress is estimated.

Using this technology, residual stresses in 316L SS and AISI 4140 are assessed after machine and stress relief annealing. This is destructive testing, where electrochemical etching is used to remove consecutive layers, and the depth of the layer removed is measured.



Figure 2.9 XRD measurement of residual stress

Parameter	Value	
Diffraction condition	Cr K radiation 18 kV, 4 mA	
Wavelength	2.291 nm	
Beam angle	156.08	
Beam size	2 mm	

Table 2.11 Parameters of measuring residual stresses using XRD method

2.8. Fatigue testing

Fatigue testing was carried out in the LAMPA ENSAM Angers laboratory facility, utilizing an RUMUL TESTRONIC fatigue testing machine under push pull conditions. Fatigue testing was carried out at room temperature with a R = -1 and a frequency of 89 Hz. Initially, the sample diameter was carefully measured. Force was then computed based on the needed stress level. Compressed air was supplied to mitigate the effects of self-heating. A thermocouple was connected to the sample to determine the effect of self-heating.

Fatigue testing was conducted using the Locati method. The fatigue limit for each material was determined using the literature study. When using the Locati approach, fatigue testing began at a lower stress level than the fatigue limit. Fatigue testing was conducted for 10^6 cycles. When failure did not occur, the stress step was raised by 25 MPa.

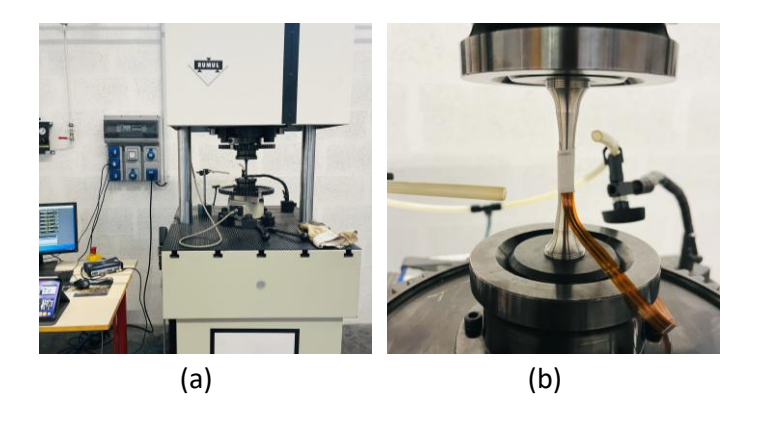


Figure 2.10 a) Fatigue testing apparatus b) mounting of fatigue sample

Crack initiation and propagation were identified using the frequency drop of testing device. Then sample was demounted from fatigue testing machine. Then crack location was analyzed using the optical microscope and the X-ray profile meter. Then sample was broken using testing and fatigue loadings. Failure surface was analyzed by suing Scanning electron microscope after cleaning the failure surface.

Chapter 3

Machining

3.1. Tool characterization

Before machining, tool angles were measured using an Alicona microscope for each insert. Alicona is a focus variation microscope. Each angle was examined three times, with averages for each machine tool. These tool angles were utilized to modeling the machining process which is crucial in accuracy of model.

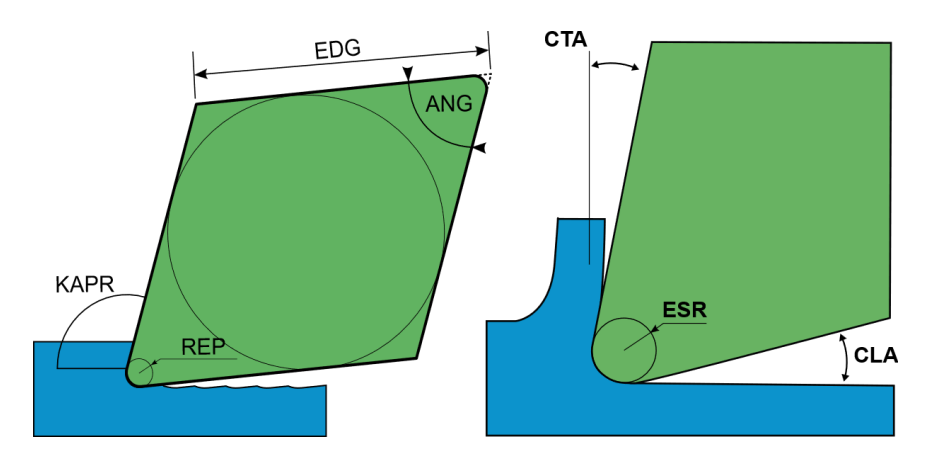


Figure 3.1 Tool geometry terminology

	DNMG150608 PF 4315	DNMG150608 QM 235	
REP (μm)	804	819	
ANG	56.4129	53.7012	
KPR	63.2670	64.0431	
СТА	1.9250	8.0674	
CLA	8.8330	9.2524	
ESR (µm)	62	51	
EDG (mm)	14	14	

Table 3.1 Measured tool geometry of DNMG 150608 PF 4315 and DNMG 150608 QM 235 $\,$

3.2. Cutting forces analysis

MATLAB was used to extract and evaluate cutting forces throughout the machining process. During machining, cutting forces are particularly critical in the thin portion of the fatigue sample. This area has the highest stress in the fatigue sample. Machining modelling was done on this fatigue sample segment. So, the machining forces of the thin portion are carefully isolated from the main signal and filtered with a moving average filter. The cutting force, penetration force, and feed forces were collected from the dynamometer and examined.

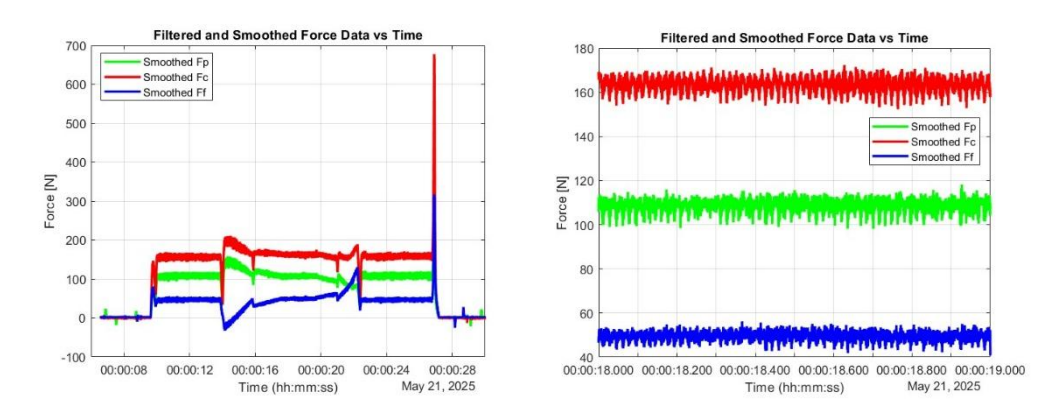


Figure 3.2 Machining forces of AISI 4140 sample 5 b) Filtered machining forces of thin section of fatigue sample of AISI 4140 sample 5

Material	Cutting force (N)	Penetration force (N)	Feed force (N)
316L SS	103	94	29
AISI 4140	167	109	51

Table 3.2 Machining forces of AISI 4140 and 316L SS

3.3. Geometrical surface state of the samples

The Alcona focus variation microscope examines the geometrical surface condition of materials following machining and heat treatment. After scanning, the findings were processed and retrieved using Mountain Maps software. Each heat-treated and non-heat-treated sample had its geometrical surface condition analysis. In this study, the geometrical surface of fatigue samples is examined in thin sections. The primary surface parameters examined are Ra and Rz.

Samples	Ra	Rz
316L machined	1.975	9.197
316L machined and heat treated	1.763	7.488
AISI 4140 machined	1.791	8.064
AISI 4140 machined and heat treated	1.571	6.261

Table 3.3 Geometrical surface state of samples measured by Alicona microscope and simulated by mountain maps software

3.4. Tool wear analysis

Optical and Alicona microscopes were used for performing tool wear assessments. The tool wear analysis requires three different measures. The parameters include flank wear (Vb), relief angle (α -Vb), and edge sharpness radius (ESR). The finishing step for each sample was carried out using a different insert. Following each completing operation, the tool was removed and kept for tool wear analysis, which is required for the simulation.

3.4.1. Flank wear (Vb)

Flank wear is defined as the average wear occurred within the flank face of insert from the rake face. Optical microscope is used for measuring flank wear.

3.4.2. Relief angle (α -Vb)

 α -Vb angle refers to the angle deviation of flank face due to flank wear. This flank wear is measured carefully using the Alicona microscope.

3.4.3. Edge sharpness radius (ESR)

Edge sharpness is defined radius of its edge. The edge sharpness increases as the tool wears. The edge sharpness is assessed using an Alicona microscope.

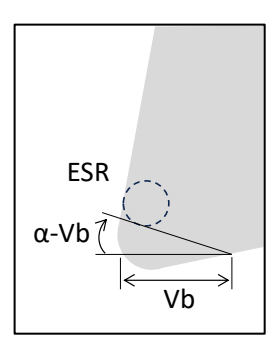


Figure 3.3 Terminology used for describing tool wear

Tool angles were measured for all 16 inserts which used for semi finishing and finishing and then averaged.

Tool	Vb (μm)	α-Vb (degree)	ESR (μm)
DNMG 150608 PF 4315	17.063	0.802	51.04
DNMG 150608 QM 235	66.984	3.03	101.39

Table 3.4 Average tool wear measurements of inserts

During tool wear measurement, it was discovered that the tool DNMG 150608 QM 235 used to process 316L SS had a built-up edge. This is because the machining was carried out at a moderate cutting speed, as shown in Table 3.4. As a result, measuring the edge sharpness radius proved difficult. As a result, ESR measurements were performed as an average of a vast surface's edge sharpness radius.

3.5. Modelling of Machining

The commercially available MISULAB software has been utilised for simulating residual stress. MISULAB employs a multi-scale approach for simulating 3D residual stress. The methodology for collecting numerical residual stresses is explained in chapter 1.3.

After completing all the trials, 3D modelling simulations were performed with the commercially available program MISULAB. This simulation was run for two machining procedures involving AISI 4140 and 316L SS. Table 2.2 and Table 2.3 include information on the material characteristics used in this AISI 4140 simulation. Plasticity parameters were determined in accordance with the Johnson cook parameters. Johnson's cooking specifications are for AISI 4140.

$$\sigma_{eq} = \left[A + B \cdot \epsilon_p^n \right] \cdot \left[1 + C \ln \left(\frac{\dot{\epsilon_p}}{\dot{\epsilon_O}} \right) \right] \cdot \left[1 - \left(\frac{T - T_O}{T_m - T_O} \right)^m \right]$$
 (3.1)

Figure 2.2 depicts the 316L experiment behavior, and the materials parameters employed are listed in Table 2.2 and Table 2.4. The tool geometries utilized for simulation are listed in Table 3.3.

3.5.1. Modelling of machining of AISI 4140

Machining was modelled using the machining parameters listed in Table 2.10. A series of orthogonal cutting operations were done to uncut chip thickness $h(1)=10 \mu m$, $h(2)=60 \mu m$, $h(3)=110 \mu m$, $h(4)=160 \mu m$, and $h(5)=210 \mu m$ in order to get a 2D equivalent loading of heat flux density (HFL, W/mm²), tangential pressure (σ_{12} , MPa), and normal

pressure (σ_{22} , MPa). Machining forces were determined using the Abaqus simulations $F_{Y\text{-TOT}(NUM)}$ and $F_{Z\text{-TOT}(NUM)}$.

The tool angles of DNMG 150608 PF 4315 are utilized for simulation, and the geometry of the tool is shown in Table 3.3. There are some tool wears within the tool, but it is minimal. Flank wear is smaller than edge sharpness radius. Since tool wear was ignored in the simulation.

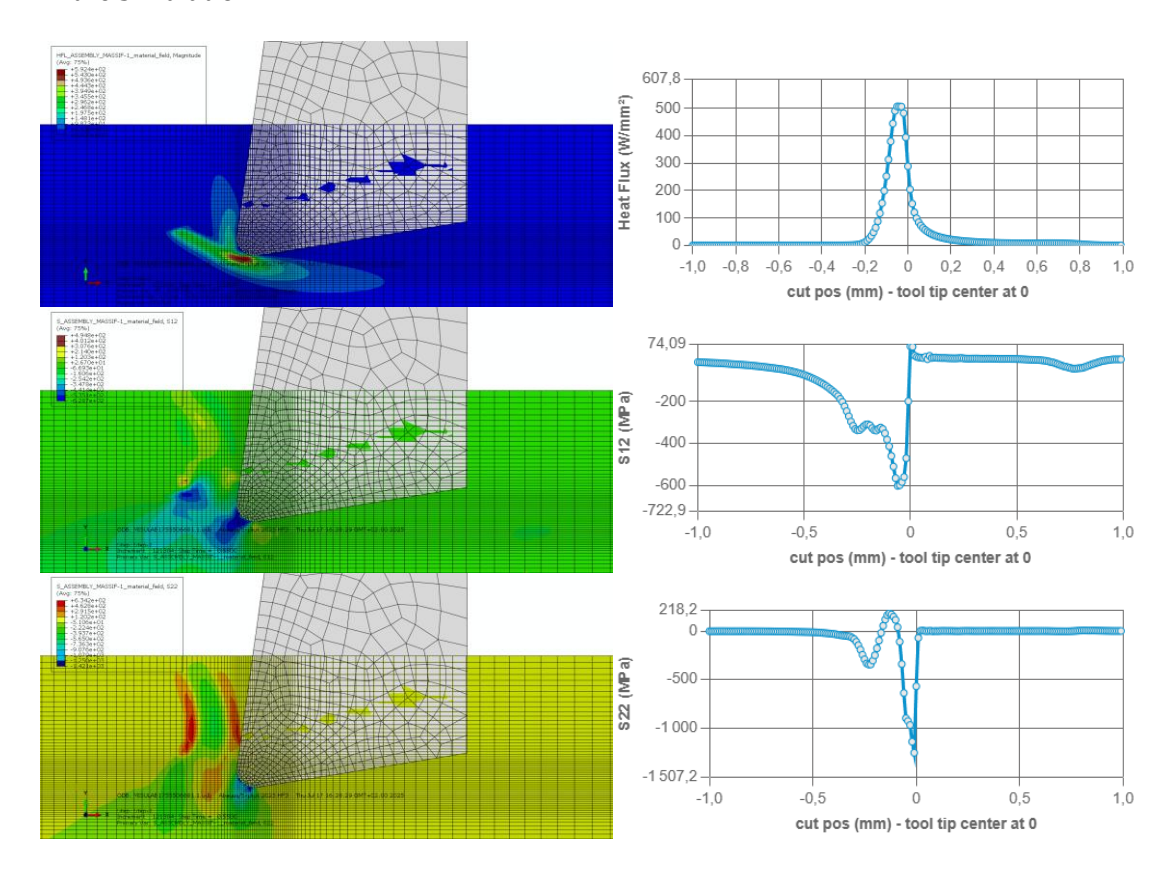


Figure 3.4 a) Orthogonal cutting operation performed for AISI 4140 for uncut chip thickness h(3) b) Heat flux density c) Tangential pressure d) Normal pressure extracted through extraction line.

The friction and heat partition between tool and workpiece are estimated using equations (1.5) and (1.7). The calculated friction and heat partition coefficients are 0.267 and 0.854, respectively.

The computed 2D equivalent thermos mechanical loadings were applied via the groove machined surface. 3D thermos mechanical loadings were computed from 2D thermos mechanical loadings using an orthogonal cutting operation and interpolated. Following the correction procedure, numerical forces were calibrated using the experimental forces and their ratios.

	Experimental	Numerical	Gain
Cutting force	167	151	1.1
Penetration force	109	71	1.5

Table 3.5 Experiment machining forces and numerical machining forces comparison for AISI 4140 cutting forces and penetration forces

After getting the 3D thermal equivalent loading, the final simulation was carried out utilizing the SYSWELD with these loadings. The 3D cutting model was utilized to generate simulated residual stress.

3.5.2. Modelling of machining of 316L SS

As mentioned in the modelling of AISI 4140, modelling of machining 316L SS is carried out. 2D orthogonal cutting operations are carried out. Machining conditions are same as mentioned in the Table 2.10. Machining tool is used is DNMG 150608 QM 235 and tool geometry is measured and mentioned in the Table 3.3.

As noted in Table 3.4, tool wear and buildup edge were discovered. The flank wear impact was ignored while calculating tool wear. Because the edge sharpness radius changed, the worn edge sharpness radius was taken into consideration. Concerning buildup edge modelling, there were two possibilities:

- 1. Extract the build-up edge surface and create a tool geometry including buildup edge
- 2. Increase coefficient of friction to have the effect of build-up edge

The friction coefficient was increased according to equation 2. The calculated friction and heat partition coefficients are 0.313 and 0.789, respectively. The following tool and material settings were used to execute an orthogonal cutting operation for uncut chip thickness: $h(1) = 10 \mu m$, $h(2) = 30 \mu m$, $h(3) = 50 \mu m$, $h(4) = 70 \mu m$, and $h(5) = 90 \mu m$.

The friction coefficient and heat partition coefficient between the tool and workpiece are computed as previously described using equations (1.15) and (1.17), yielding values of 0.313 and 0.828, respectively.

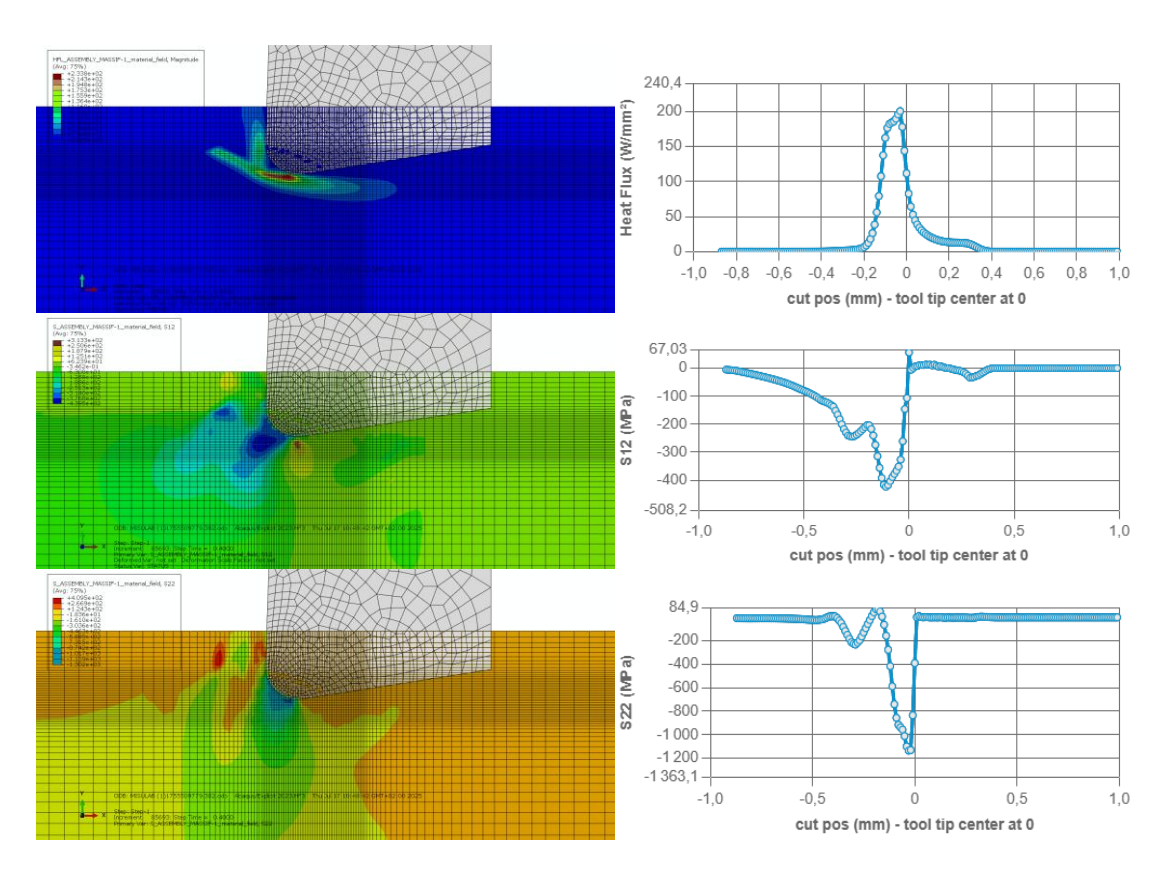


Figure 3.5 a) Orthogonal cutting operation performed for AISI 4140 for uncut chip thickness h(3) b) Heat flux density c) Tangential pressure d) Normal pressure extracted through extraction line.

	Experimental	Numerical	Gain
Cutting force	103	66	1.6
Penetration force	94	65	1.4

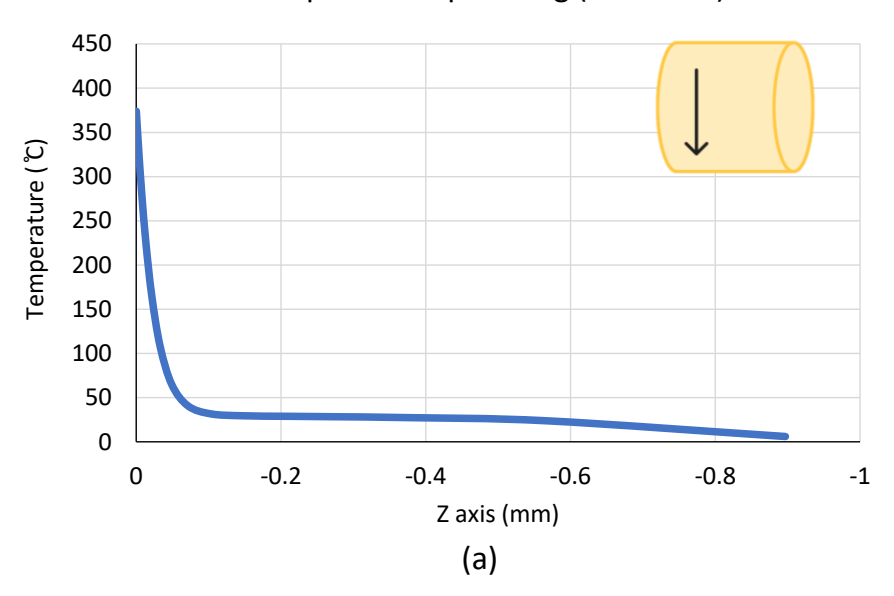
Table 3.6 Experiment machining forces and numerical machining forces comparison for 316L SS cutting force and penetration force

Further modelling was carried out as explain in the modelling of AISI 4140 in Modelling of machining of AISI 4140.

3.5.3. Simulation results

After executing the 3D SYSWELD cutting model, the results were obtained. When the tool moves ahead in the cut direction (Y), the surface temperature rises due to thermomechanical loadings. Temperature spreading may be predicted by simulating the tool ahead at its position. This gives an insight into the thermally impacted layer.

Temperature spreading (AISI 4140)



Temperature spreading (316L SS)

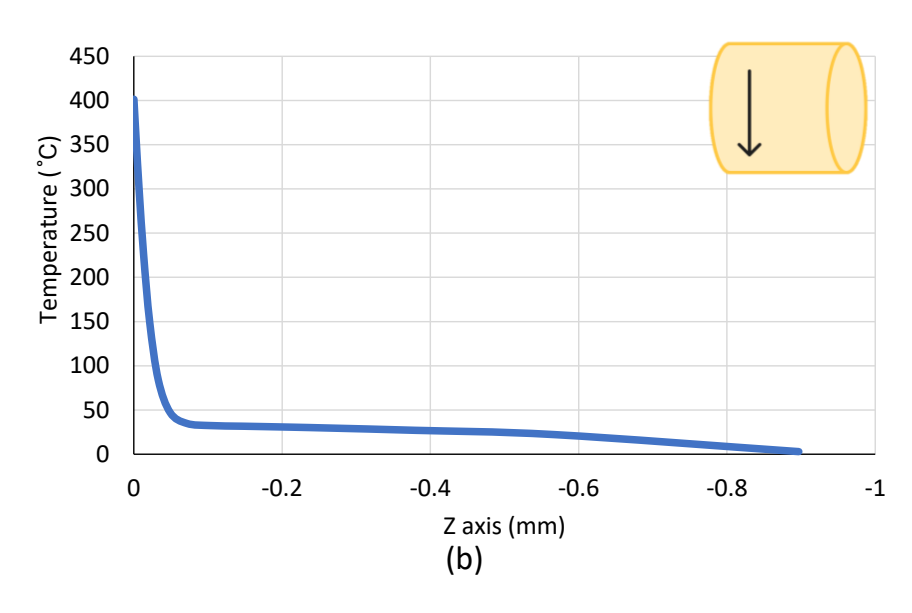
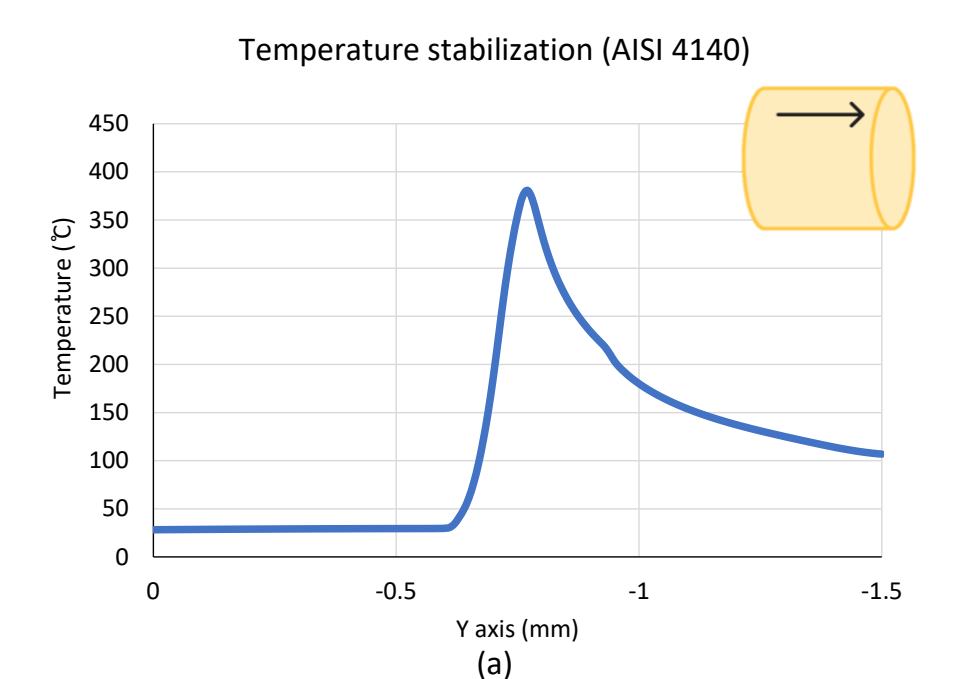


Figure 3.6 Temperature spreading a) AISI 4140 and b) 316L SS

According to the numerical simulation based on the specified material parameters and cutting circumstances, the thermally impacted layer for both 316L SS and AISI 4140 is 0.4 mm.



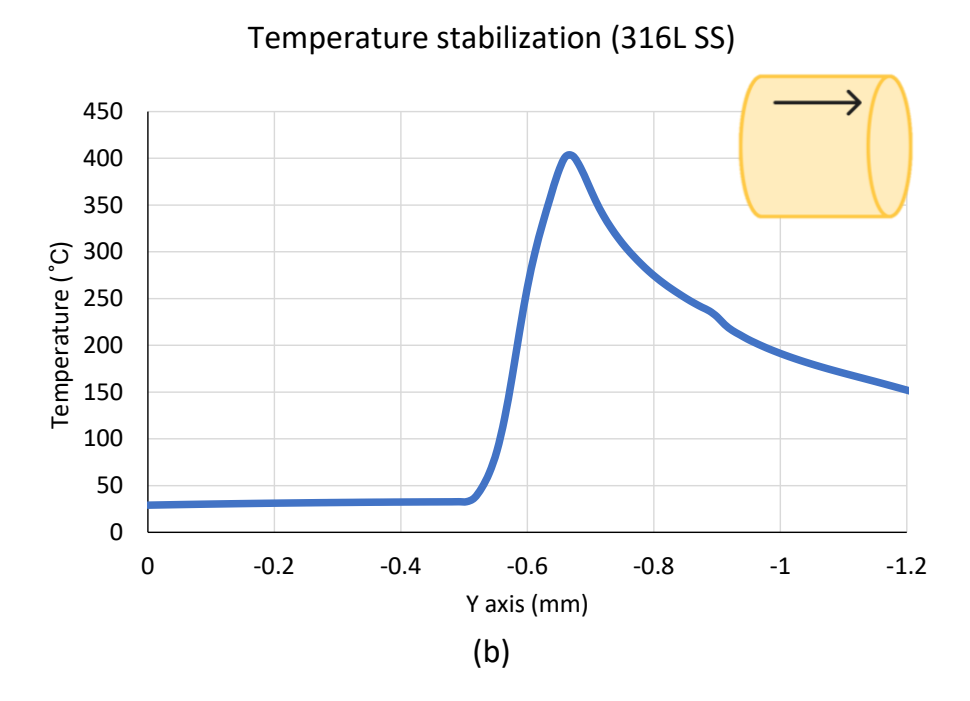


Figure 3.7 Temperature stabilization a) AISI 4140 and b) 316L SS

The temperature distribution in the surfaces rises with each spin of the tool. When the tool contacts the workpiece's surface, the surface temperature rises owing to thermomechanical loading. The temperature stabilization data is derived from the FEA model. According to the numerical model, for certain material qualities and machining circumstances, the surface temperature of 316 rises to a maximum of 402 $^{\circ}$ C, while that of AISI 4140 is 380 $^{\circ}$ C.

3.5.4. Modelling of Residual Stress

The residual stress was simulated using a FEA model, and the part was cooled down to room temperature. Results gathered from two revolutions preceding the last revolutions. Average values were achieved between the peaks and valleys. The resulting residual stress curves were then compared to the experimental data.

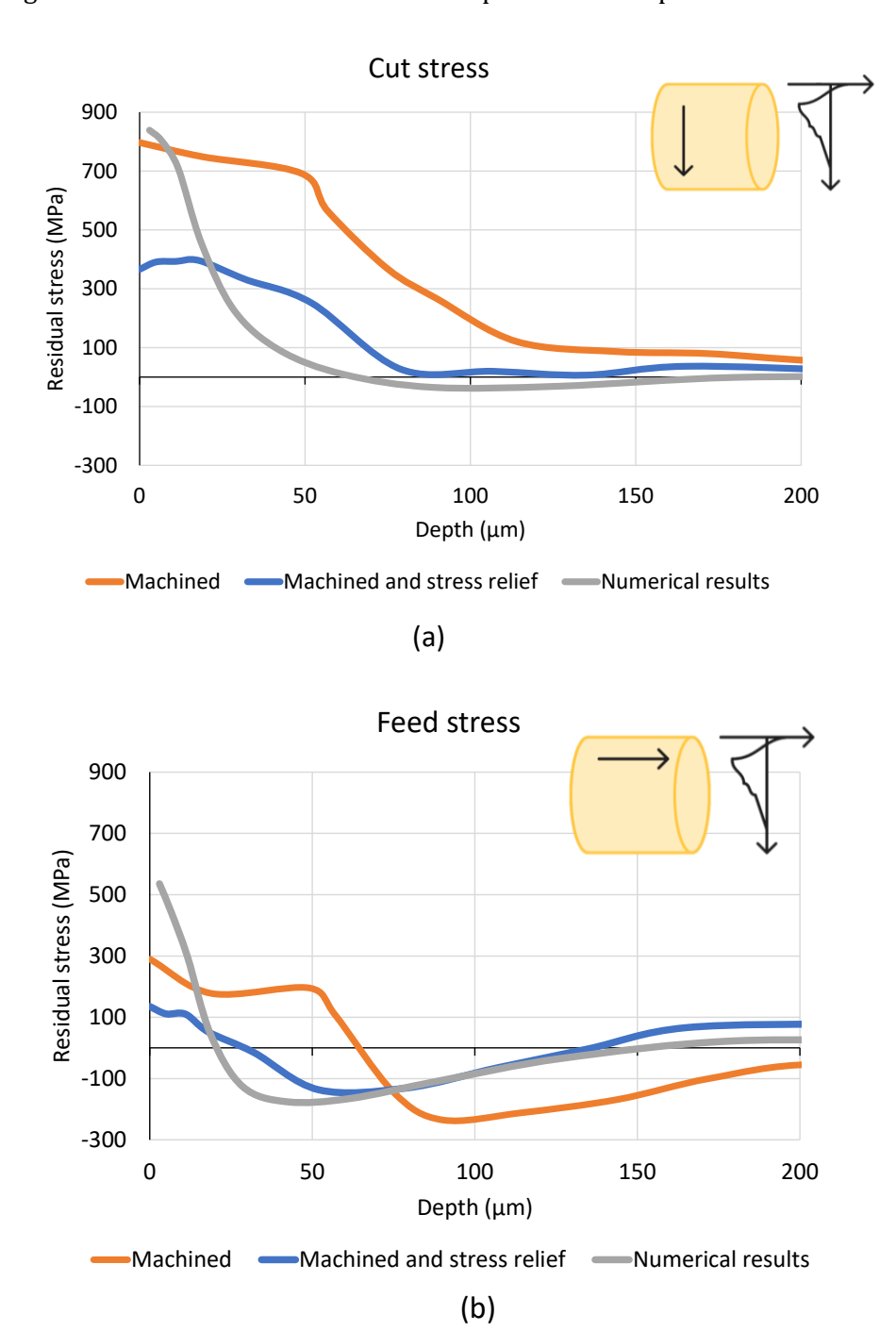
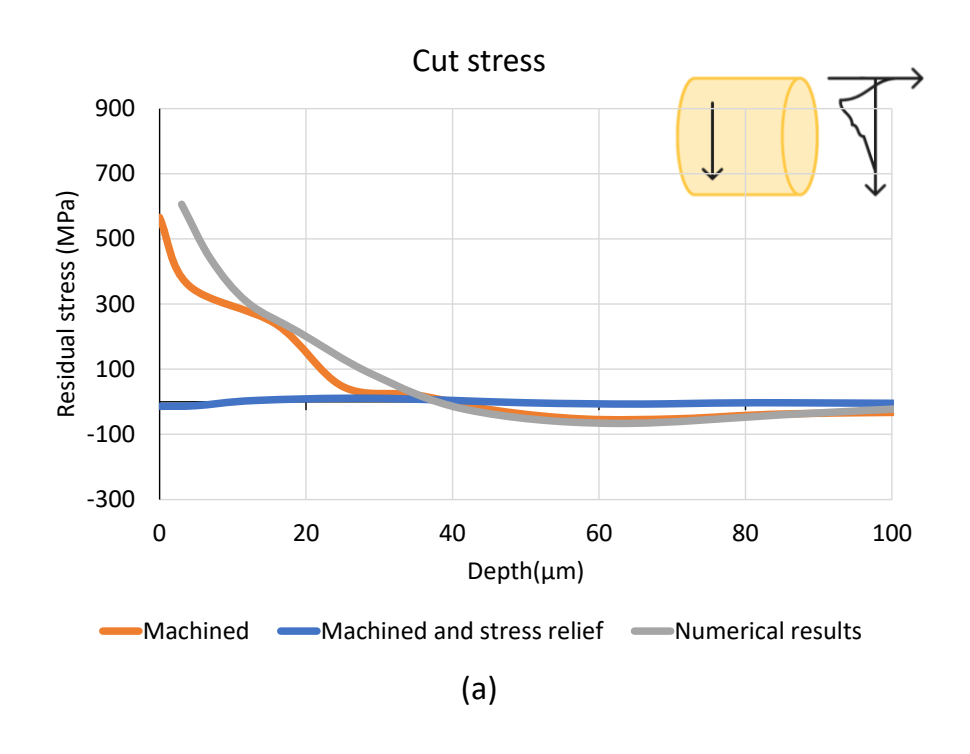


Figure 3.8 Residual stress of 316L SS a) Cut stress b) Feed stress



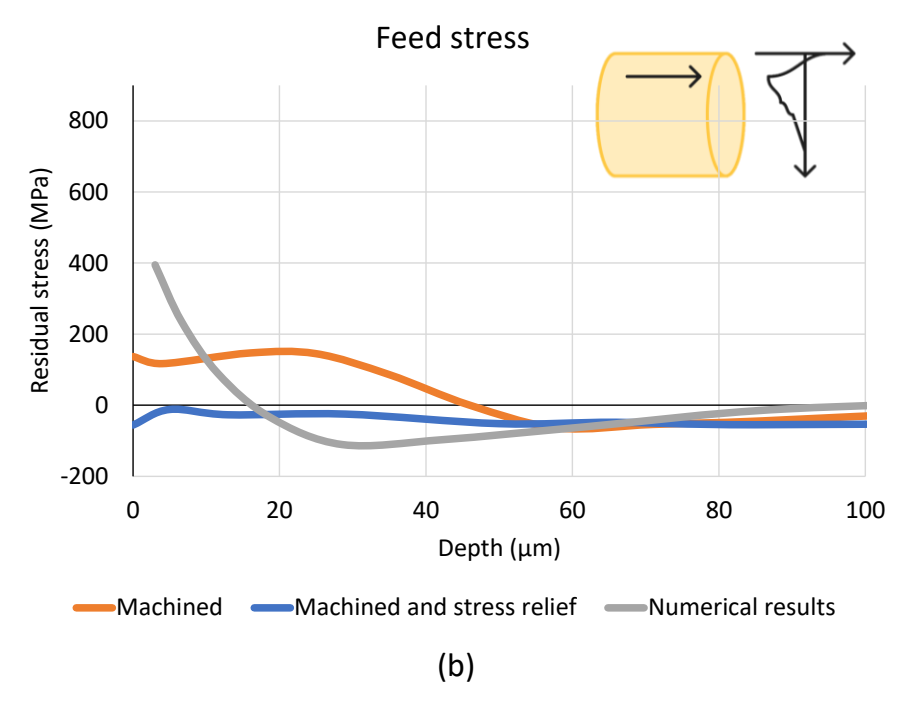


Figure 3.9 Residual stress of AISI 4140 a) Cut stress b) Feed stress

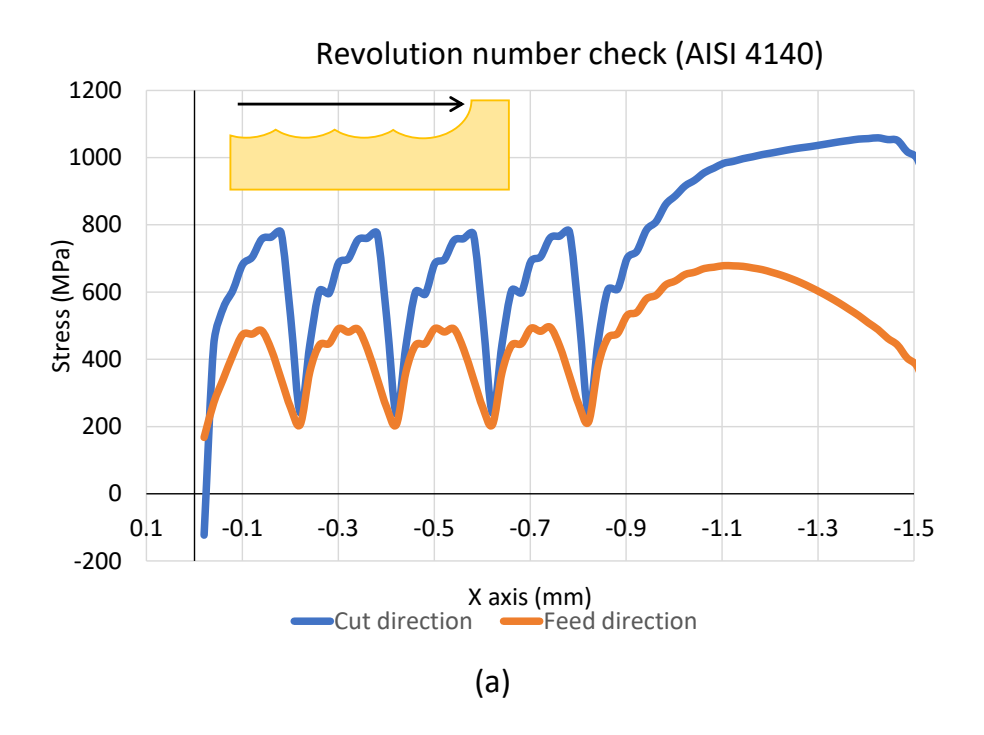
The computational results for AISI 4140 residual stress and numerical stresses were compared to experimental data. XRD data show that stress relief annealing decreased residual stress in AISI 4140 and 316L stainless steel. It has been demonstrated that stress relief annealing of AISI 4140 is quite effective.

The contour of the XRD measurement findings of machined 316L SS samples is not what was expected. Furthermore, the XRD test of AISI 4140 in the feed direction did not yield the predicted curve. For 316L SS, residual stresses at the workpiece's surface are virtually flat at 50 μ m. Similar behavior reported for AISI 4140 at a depth of 27 μ m. Error of residual stress on surface was calculated and mentioned below.

Errors	Cutting	Feed
316L	5.27%	84.83%
AISI 4140		
dewminisiriwardhana@gmail.com	7.07%	188.32%

Table 3.7 Comparison of residual stresses of experimental and numerical of surface

Extracted results indicate that results are stabilized at cut direction. Stresses are not stabilized at the corner due to boundary conditions.



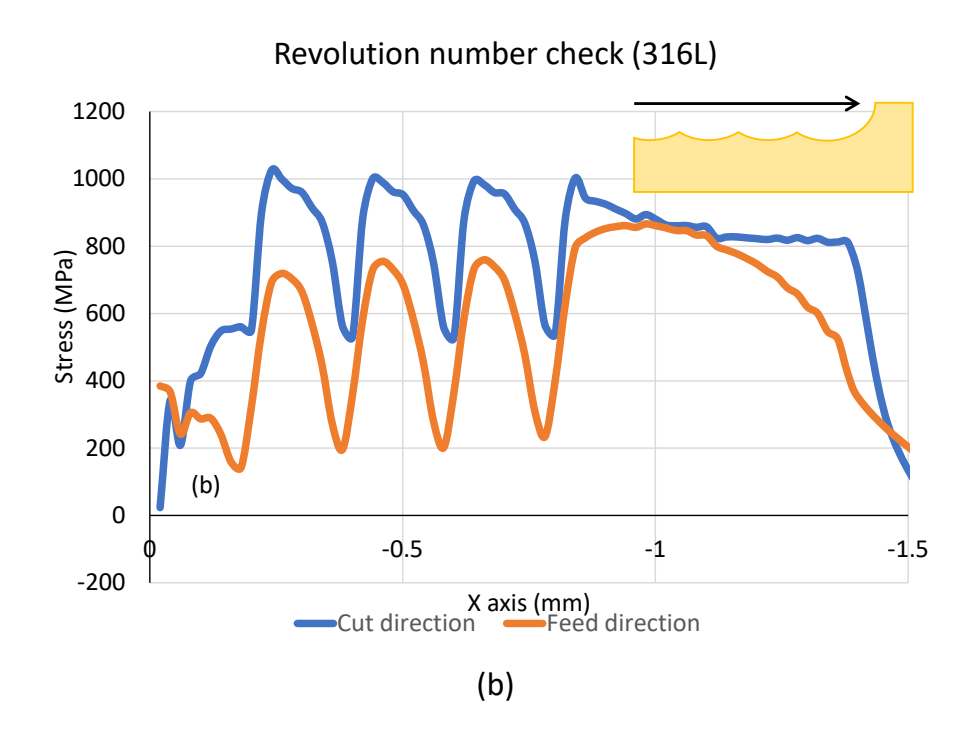


Figure 3.10 Revolution number check a) for AISI 4140 b) for 316L SS

The simulation ran for 8 revolutions, with results collected from the final 5 revolutions. Results were extracted when the material was cooled to room temperature. The residual stresses of peaks and troughs are clearly different.

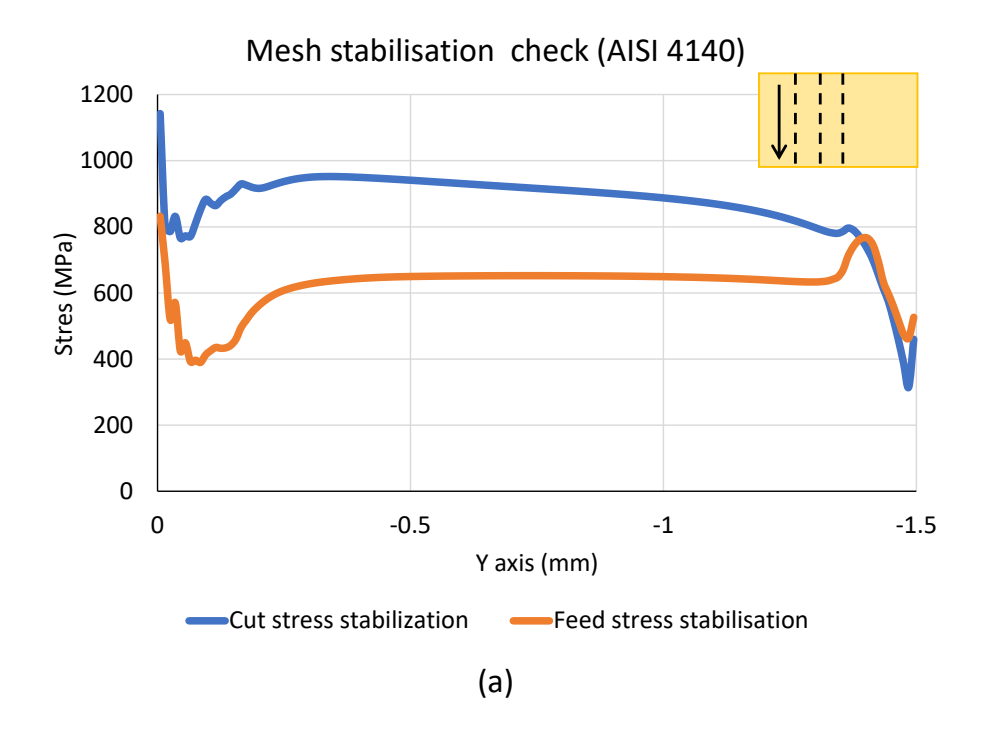
	Cut stress (MPa)		Feed stress (MPa)			
	Peak	Valley	Difference	Peak	Valley	Difference
AISI 4140	776	239	537	491	208	283
316L SS	1007	532	475	745	210	534

Table 3.8 Residual stresses of peaks and valleys of groves

Experimental residual stress curves diverge from numerically predicted findings. However, the cut-direction model successfully predicted the surface's residual stresses.

The stress on the cut direction (Y axis) and feed direction (X axis) was verified to ensure that the numerical results were stable. Surface stresses in the cut direction must be stabilized following tool movement and cooling. This is why the strains in the cut and feed directions were tested in the Y axis during the last revolution. The feed dimension surface is made up of grooves. According to Earlies, residual stress varies throughout

the groves in peaks and valleys depending on the grove's site. This data obtained by FEA simulations. These data give information about the model's stability.



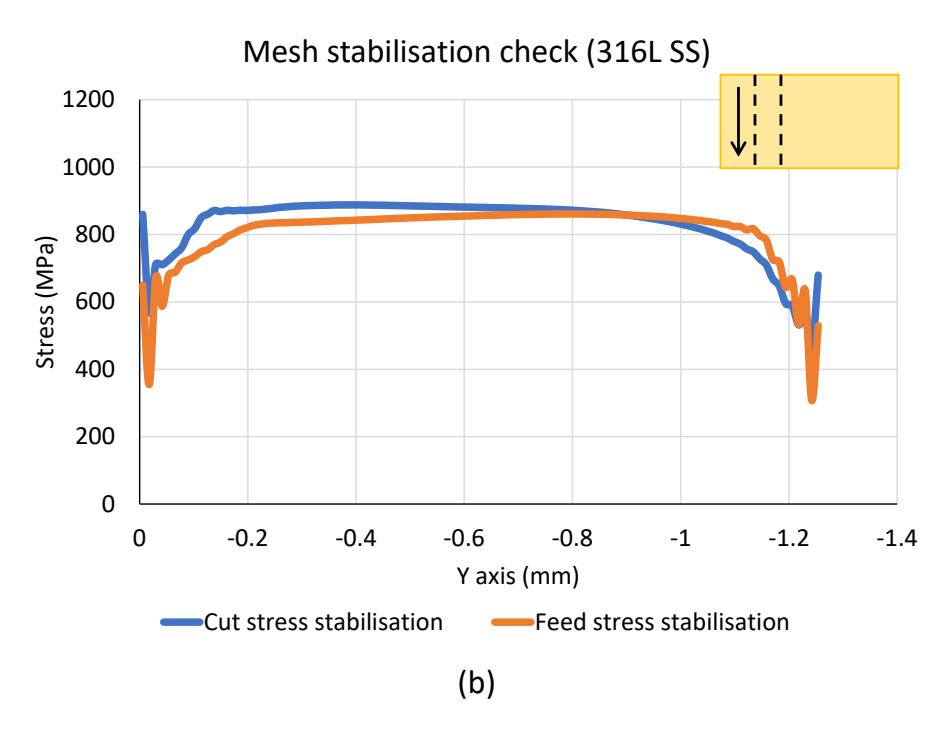


Figure 3.11 Mesh stabilization check

3.6. Theoretical, Numerical and Experimental chip correlation

Following each completion process, chip samples were obtained for the chip experimental numerical correlation.

Long tightly coiled spiral shaped chips made from AISI 4140 were noticed during milling. This indicates continual cutting operation. Chips became dark blue in color, indicating chip oxidation and considerable heat generation during machining. The chips also have extremely minute serrations. During the machining of 316 L, lengthy continuous chips were observed, as is common for ductile material.

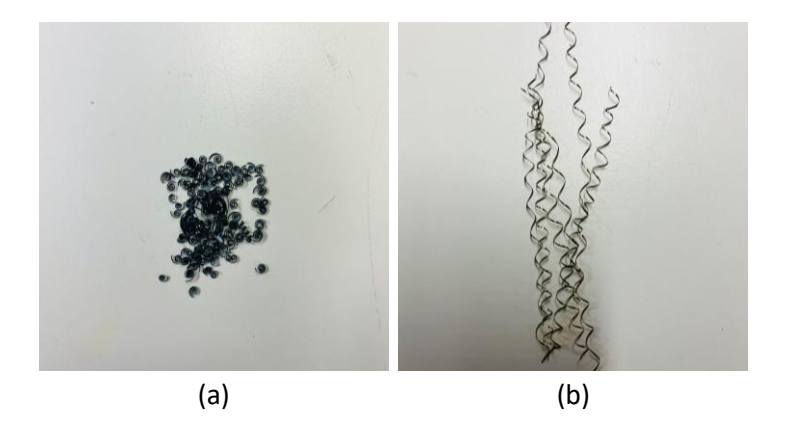


Figure 3.12 Chip sample collection of a) AISI 4140 b) 316L SS



Figure 3.13 Experiment chip section of a) AISI 4140 and b) 316L SS

The numerical model's validity was tested using theoretical, numerical, and experimental chip correlation. A 2D design of an uncut chip section was constructed, and the locations of those uncut thicknesses were determined using the simulated uncut chip thicknesses, as well as angle fractions. The angle fractions of deformed chip thickness

were computed using image correlation of a chip portion. The thicknesses of the distorted chips were then compared to those created using the orthogonal cutting model.

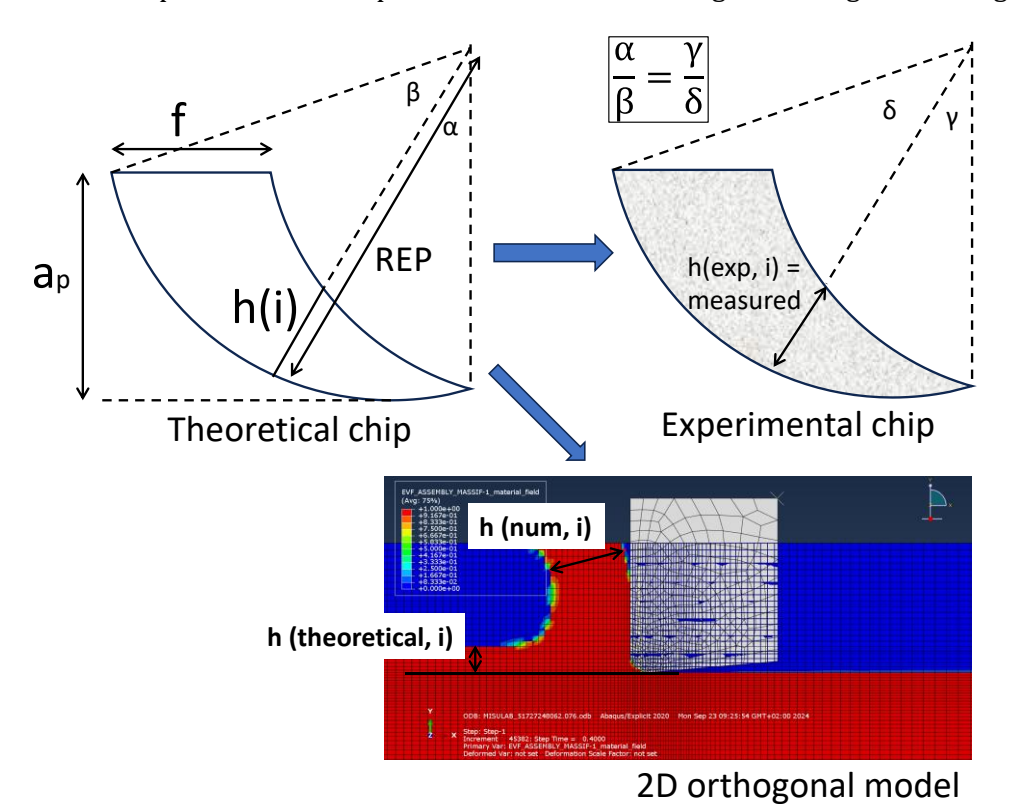


Figure 3.14 Methodology of theoretical, numerical and experimental chip correlation

SI No.	h theoretical (μm)	h experimental (μm)	h numerical (μm)	Relative error
1	90	221.604	181.07	-18.29%
2	70	177.2517	149.45	-15.68%
3	50	130.0126	100	-23.08%
4	30	78.6794	60	-23.74%
5	10	26.55889	28.14	5.95%

Table 3.9 Theoretical, experimental and numerical chip correlation for 316L SS

SI No.	h theoretical (μm)	h experimental (μm)	h numerical	Relative error
1	140	302.372	281.663	-6.85%
2	120	264.4836	244.78	-7.45%
3	70	184.9811	147.41	-20.31%
4	30	89.47313	78.65	-12.10%
5	10	31.80101	25.27	-20.54%

 $Table\ 3.10\ Theoretical, experimental\ and\ numerical\ chip\ correlation\ for\ AISI\ 4140$

This theoretical, experimental, and numerical chip thickness correlation shows that the difference between numerical and experimental chip thickness is less than 20%. This proves that the cutting model is both valid and precise.

Chapter 4

Fatigue Testing and modelling

Following the acquisition of regulated surface integrity values for both materials, the specimens underwent fatigue testing to analyze their fatigue behavior.

4.1. Conducting fatigue experiments

4.1.1. AISI 4140 machined samples testing

AISI 4140 is a material with brittle behavior. Thus, the fracture beginning spots were easily identifiable. An optical microscope was used to investigate the initiation of crack. When fracture start was identified using the frequency of the fatigue testing equipment, the sample was extracted and examined under an optical microscope. The sample was then rotated by hand to get images of the top and bottom of the crack. Figure 4.1 depict the fracture distribution in the material as detected by the optical microscope.

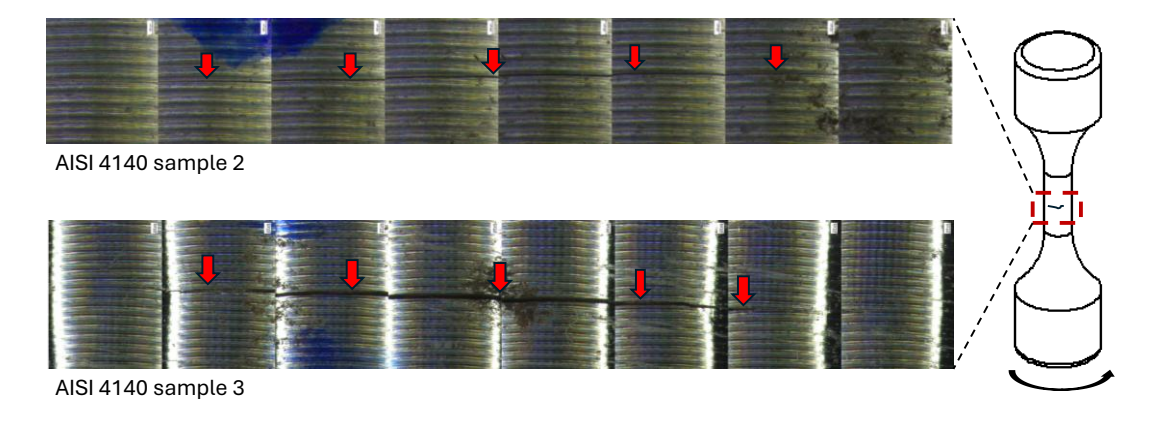


Figure 4.1 Optical microscope observation of crack of AISI 4140

Initially, cracks were examined using an optical microscope.

After that, a crack dispersion site was determined using an X-ray profilometer. The crack was scanned using the X-ray profilometer, just as the optical microscope. The sample was rotated, and pictures were obtained from the X-ray profilometer. The back scan and length were set at $300\mu m$. Tilt and cylindricity removal filters were employed for the final imaging.

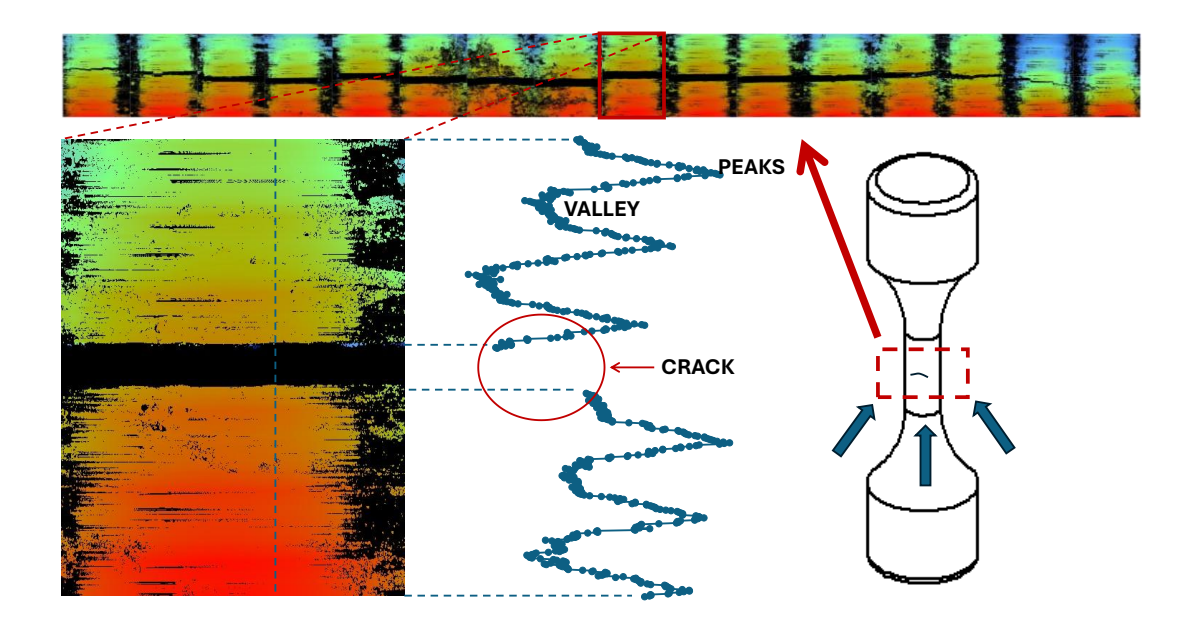


Figure 4.2 X ray profilometer scan of crack of AISI 4140 sample 3

This graphic demonstrates how fractures are distributed inside a grove and do not move from one grove to another via the grove's top. The profilometer scan identified pitting corrosion in the sample. Following the profilometer evaluation, samples were broken using a mixture of fatigue and tensile tests. After profilometer measurement testing, the failure surface was evaluated under a scanning electron microscope.

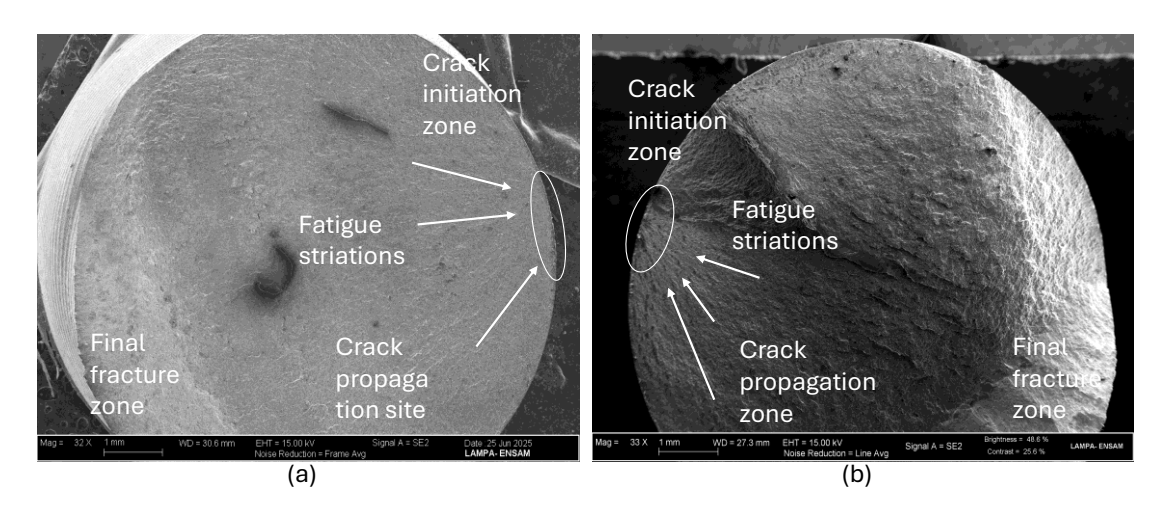


Figure 4.3 Failure surface analysis of AISI 4140 a) sample 1 b) sample 2

Analysis of the failure surface indicates three unique zones inside each fatigue failure zone. These are the crack initiation, propagation, and final fracture sites. Crack initiation often happens in a notch, inclusion, or other type of surface defect. Crack initiation sites are often near the surface. This is indicated by fatigue striations in the fracture propagation zone. Fatigue striations are often aligned with the fracture's beginning

position. The fracture propagation zone is flat surface. It is located between the crack initiation point and the final fracture site. Crack proportion sites seem smoother and more textured than initiation sites. The final fracture zone is called the overload zone. The final fracture zone occurs when the remaining cross section falls abruptly. The last failure zone has a rough and uneven surface.

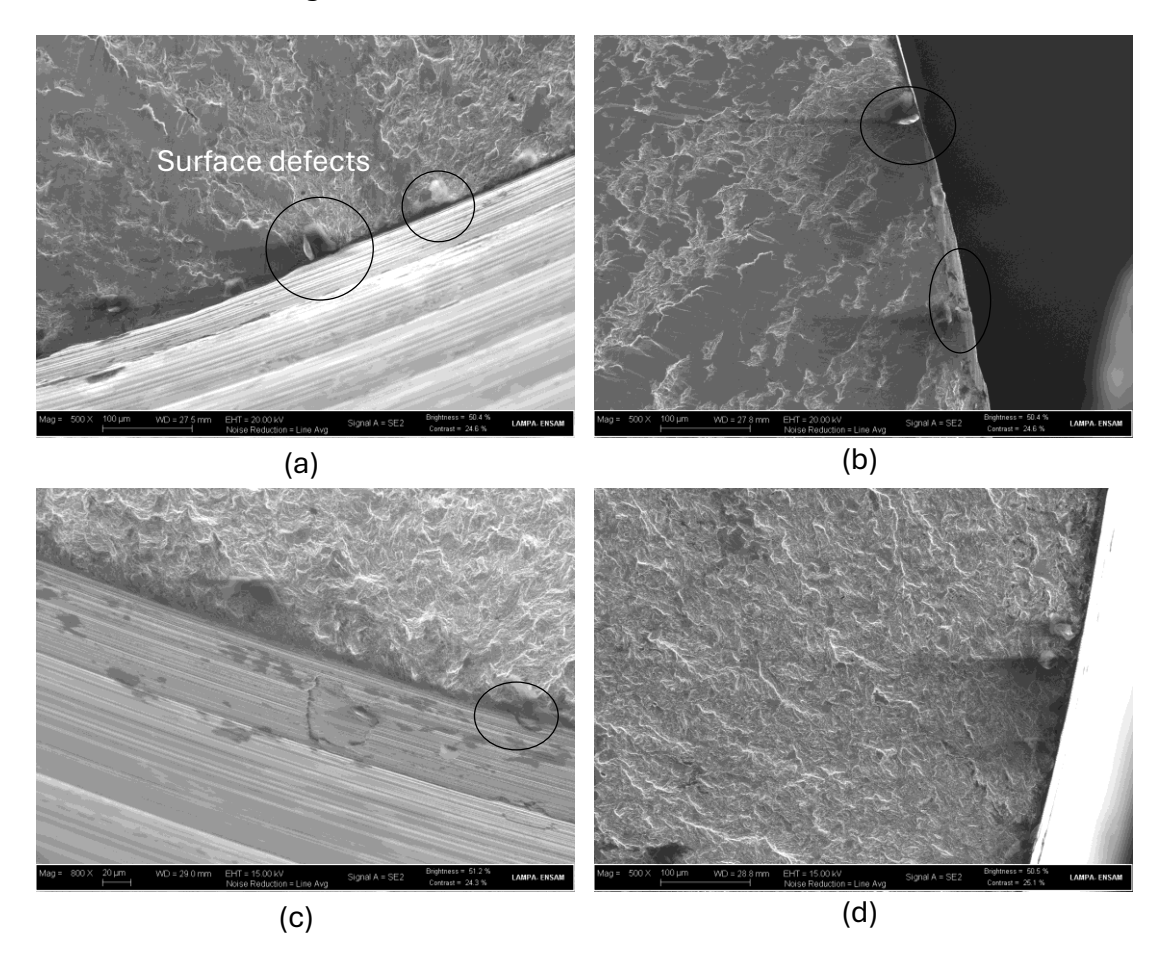


Figure 4.4 Crack initiation sites of AISI 4140 a) b) sample 1, c) d) sample 2

When cracks are examined attentively, it is obvious that they come from the grove valley spots in samples 1 and 2. Surface defects are the primary target of fatigue striations. These flaws appear to have developed because of pitting corrosion or material removal during machining processes. This is clearly obvious in sample 1. The fracture initiation site consists of several pits, the origins of which are unknown. Surface defects may be detected in the fracture initiation locations of AISI sample 2. These surface faults are highlighted in the figures.

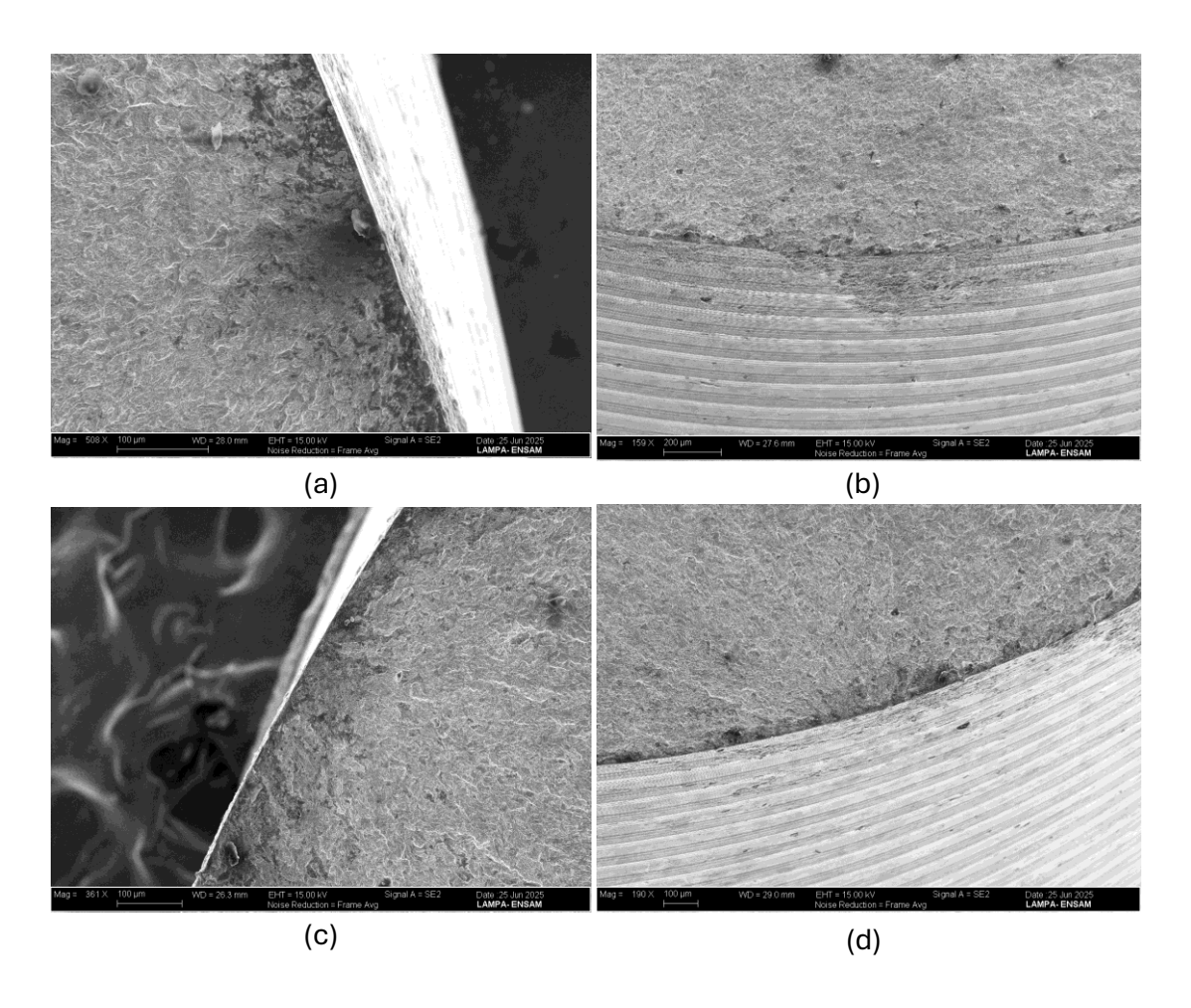


Figure 4.5 Crack initiation site of AISI 4140 sample 3

In the fracture initiation site of AISI sample 3, corrosion and surface flaws are found. This creates uncertainty about which causes crack initiation in the sample. But what is noteworthy is how the fracture spreads down the valley of the grove.

EDS analysis was done to investigate the crack initiate point of AISI 4140 sample 1 and to better understand the chemical composition dispersion. The crack initiation location exhibits an equal distribution of Fe, Cr, and Mn. These components are included in the alloy composition. Pit geometry may be validated using the iron distribution of Fe. The pit site has an equal distribution of O. Oxygen is an element that implies rusting. When there is Oxygen, it means there are oxides. However, there is no indication of Oxygen around the pit, confirming that the crack was not triggered by corrosion pits. Carbon indicates foreign materials, such as dust. Carbon is seen near the pits. This shows that holes include foriegn materials such as dust.

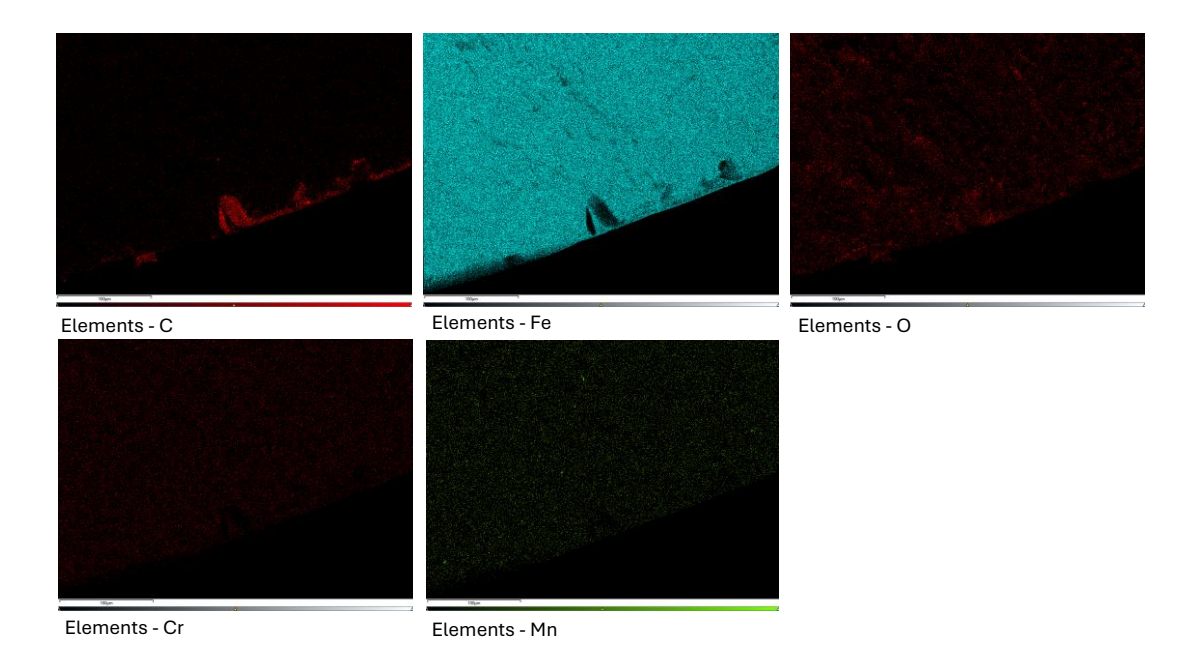


Figure 4.6 EDS analysis of crack initiation site of AISI 4140 sample 1

This EDS examination proved that fissures are caused by machining flaws, not corrosion. The chemical composition of pit locations reveals that the pits of crack initiation sites contain less oxygen. This demonstrates that fractures are caused by surface imperfections that arise during machining, rather than corrosion.

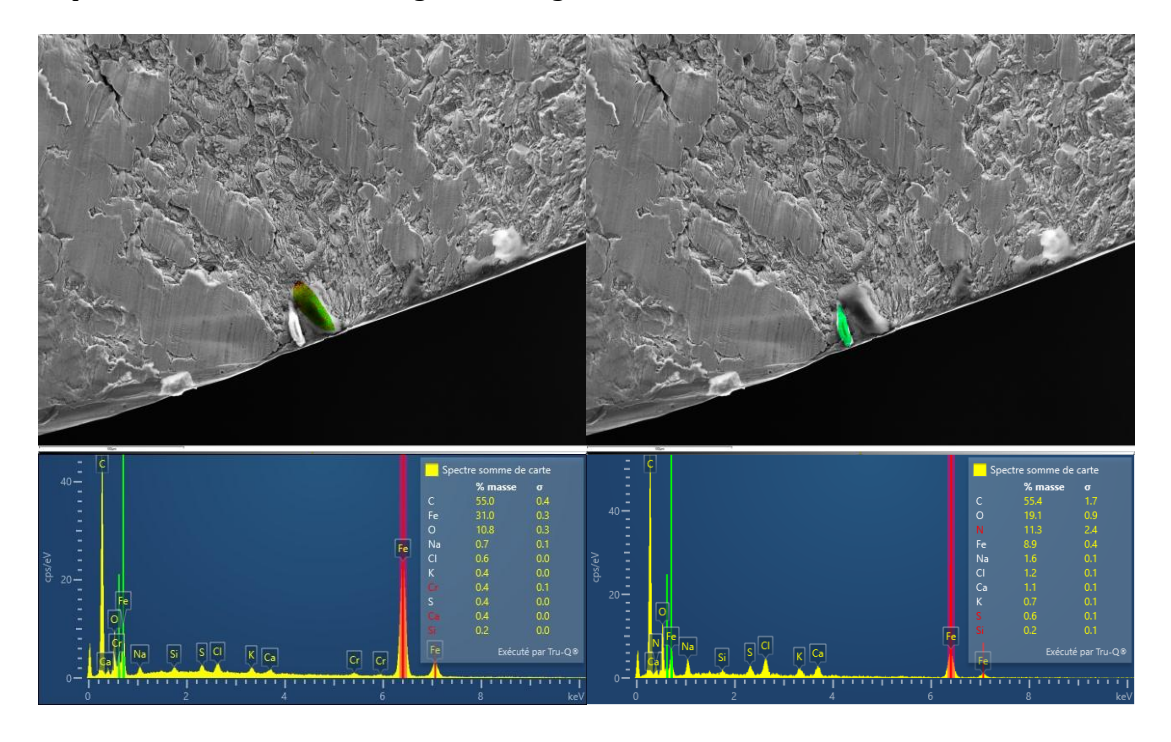


Figure 4.7 Chemical composition of AISI 4140 simple 1

4.1.2. AISI 4140 Machined then stress relieved samples testing

Fatigue tests were conducted on both machined and stress relieved materials. Machined and stress relieved samples had a longer fatigue life than AISI 4140 machined samples under the same circumstances. Unfortunately, samples were broken from their threads, making it impossible to determine how residual stress affected fracture onset.

There might be reasons why the threads snapped rather than the thin sections of the samples. For AISI 4140, only machined and stress relief annealed samples were affected by this problem. Stress-relieving annealing is the direct source of this effect.

Stress reduction annealing was conducted in a nitrogen atmosphere rather than a vacuum environment. Because of this, oxides were present on the surface. Surface oxidation caused samples to become blue during stress reduction annealing. Stress relief annealing modified some of the material's properties, resulting in this outcome.

Stress treatment annealing was conducted to relieve residual stress in the machined component. However, residual strains near the tread may have been unaffected by the stress alleviation annealing process. And these treads may have served as a notch in the sample, increasing stress concentration. This might explain the beginning of cracks at the samples' roots.

Because AISI 4140 machined and stress relief annealed samples broke from the treads and damaged the testing equipment, the tests were abandoned with immediate effect.



Figure 4.8 AISI 4140 TTH sample 6 Failure

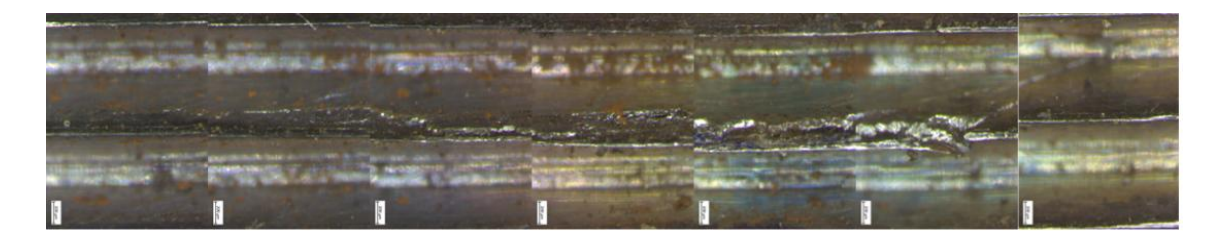


Figure 4.9 Crack propagation within the threads in AISI 4140 TTH sample 5

4.1.3. 316L SS machined and machined, stress relief annealed samples testing

316L is a more ductile material than AISI 4140. Additionally, it has lower fatigue limitations than literature. Fatigue testing was conducted under the identical conditions as for AISI 4140. When fatigue samples reach the fatigue limit, they are self-heated. Which raises the temperature of the samples by over 100 °C. When self-heating occurred, fatigue testing was stopped.

The goal of fatigue testing is to determine the exhaustion limit without self-heating. Self-heating softens the material and eliminates the influence of residual tensions. If the sample temperature exceeded 70 °C while the fatigue test was ongoing, it was halted. To lessen the self-heating effect, compressed air was supplied. However, the self-heating effect was unstoppable.

Then fatigue testing was performed for 10⁶ cycles lowering stress step to avoid self-heating. Then observed that samples were continuously hot during the stress step. During this step samples were not broken. Same happened to 316L SS stress relief annealed samples. After many attempts to break the samples, it was decided to not to move forward with 316L SS materials.

Then, fatigue testing was carried out for 10 million cycles, with the stress step reduced to avoid self-heating. The samples were then seen to be constantly heated during the stress stage. During this stage, no samples were broken. The same thing happened with 316L SS stress relief annealed samples. After many efforts to break the samples, the decision was made not to proceed using 316L SS materials.

Self-heating occurred during fatigue testing because of internal friction and plastic work dissipation. When 316L undergoes plastic deformation during cyclic loading, a portion of the mechanical energy input is lost as heat rather than being stored. However, 316L SS's less thermal conductivity means that it does not release heat as rapidly. Therefore, heat can build. Furthermore, friction may arise because of microstructure motions. During fatigue testing, movement and rearrangement of dislocations, as well as twinning

processes, may occur, contributing to energy loss. In 316L SS face centered cubic (fcc) structures, active slip systems create higher frictional movement, resulting in heat loss.

4.1.4. Failure points of AISI 4140

Since 316L SS materials did not broke due to self-heating and AISI 4140 machined and stress relief annealed samples broken from tread, Fatigue tests were not successful as it planned. However, S-N curve was plotted according to the tests performed.

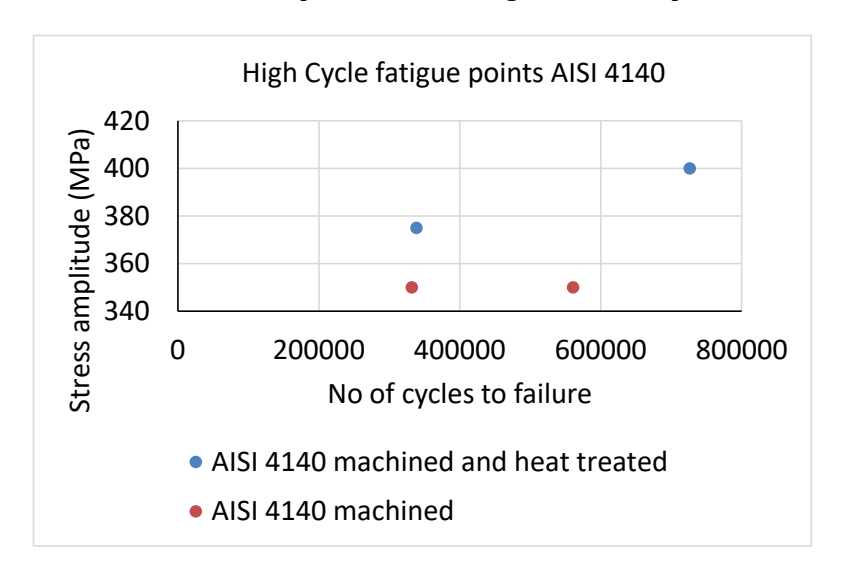


Figure 4.10 Failure points of AISI 4140

The above-mentioned SN curve shows that machined samples have lower fatigue limits than the literature by (Limodin & Verreman, 2006). Stress relief annealed samples have a longer fatigue life than machined samples. Stress alleviation annealed samples exhibit lower tensile residual stress than machined samples. It demonstrates that larger tensile residual stresses have a lower high cycle fatigue life.

4.2. Critical distance analysis

AISI 4140 is a material that is very susceptible to oxidation. During the fatigue tests, many pits were found on the surface. The problem statement is that these pits significantly modify the stress concentration on the surface of the sample, resulting in fracture initiation. This is examined by Finite Element Analysis (FEA) modelling.

First, fatigue test samples were scanned, and the profile was retrieved using an X-ray profilometer. The surface was scanned at 3X, with a length of $300\mu m$ and a back scan of $300\mu m$. The final surface was calculated by averaging two scans. The acquired surface was then filtered using a median filter (window size = 3) and a tilt removal filter (irritations = 7). Then the surface profile was extracted.

There are some obvious pits in the figure above. The first surface profile was extracted in an area where pits were not present. Then the pit dimensions were measured. The X-axis resolution for surface profiles is $1.98~\mu m$.

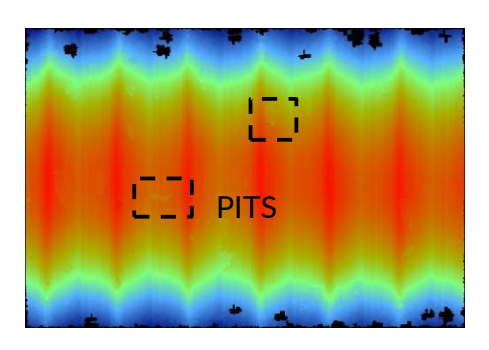


Figure 4.11 Pits observation of AISI 4140

Pits	dx (mm)	dy (mm)	dz (um)
1	0.0337	0.0286	1.3184
2	0.0277	0.0492	0.6255
3	0.0535	0.0554	1.0301
4	0.0475	0.101	0.3731
5	0.257	0.0532	0.4446

Table 4.1 Pits characterization

The extracted coordinates were transformed to a line using Python code. Then one section was made without pits. And one section was made up of pits, including measured pits that were randomly placed on the surface. The elastic and density parameters of AISI 4140 were assigned to the component listed in Table 2.2. CPS4R elements were employed for meshing, with elements close to the surface at 2 μ m resolution in the X direction. One side of the part was enclosed, while the other was subjected to 100 MPa of pressure. Then simulations were run, and the stress gradient around the pits was compared to the simulation without pits.

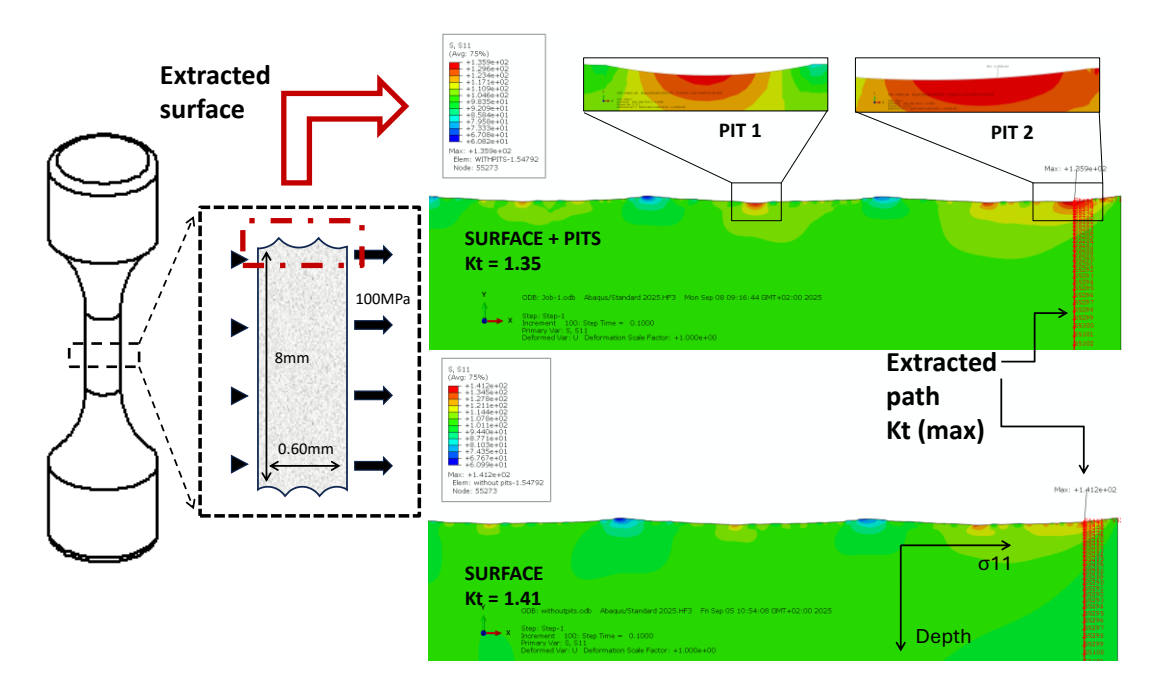


Figure 4.12 Simulation methodology

This basic simulation demonstrates the significance of stress distribution on machined surfaces. The diameters of the pits are on a microscale; yet they do not significantly affect total stress concentration. The simulation demonstrates that stress concentration consistently occurs near the valley, regardless of the presence of pits. However, stress concentration is significantly reduced at the peaks of the geometry. This indicates a reduced likelihood of fracture initiation at the peaks of the grooves. Both machined samples, regardless of the presence of pits, exhibit essentially identical stress gradient curves. Stress gradient was calculated from along the line of maximum stress concentration at the surface.

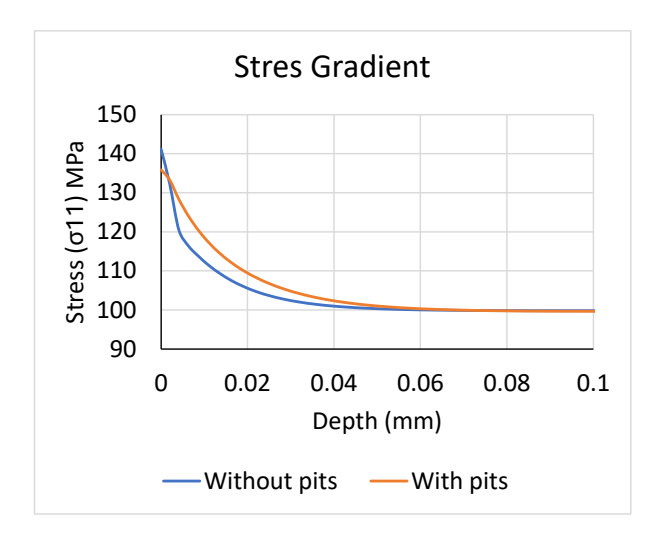


Figure 4.13 Stress gradient comparison with pits and without pits

This stress gradient is significantly less than that reported in Figure 1.3. This indicates that pits do not function as notches and do not modify the outcomes. Microscale pits create stress concentration on the surface, although they do not exert the same effect as notches.

Chapter 5

Discussion of Results

As seen in the Figure 3.8 and Figure 3.9 residual stresses curves, the model predicted the surface's residual stress. However, when it came to the whole form of the residual stresses, the model was unable to accomplish the model's residual stress shape. There might be various explanations for this situation.

The model is validated based on the results of a single experiment performed for a specific material. Several XRD measurements are required to acquire an exact hook shape for residual stresses. This can be fully proven using the two-scale technique to modelling 3D residual stresses.

During XRD tests, surface layers are removed by electro polishing to determine the residual stresses of the samples. This causes the residual stresses of the surface acquired after electro polishing to fluctuate when the mechanical balance changes. This results in fluctuations in the surface residual stresses acquired post-electropolishing when the mechanical equilibrium alters. XRD measurements were performed just once for a single category of samples. If XRD measurements were performed on a greater number of samples, the resulting curves would likely be more precise and accurate.

Heat treatments were first used to remove the sample's thermal history. For the machining procedure, 8 bars from each material were selected from a large bar. Then this bar was wire-cut. Initially, the material underwent stress relief annealing to erase the sample's thermal history. Following machining the material was subjected to stress relief annealing under the same conditions. This was done to remove the residual stress.

One assumption is that heat treatment should not change the material's microstructure or mechanical characteristics but instead minimize residual stresses. There are a few causes for residual stress in machined materials to differ from the hook shape: stress relief annealing affects the microstructure or mechanical properties of the samples.

Initial condition	Machined	Machined and heat treated
(0.3 HV)	(0.3 HV)	(0.3 HV)
344.6	309.7	333.7

Table 5.1 Comparison of microhardness measurements of AISI 4140

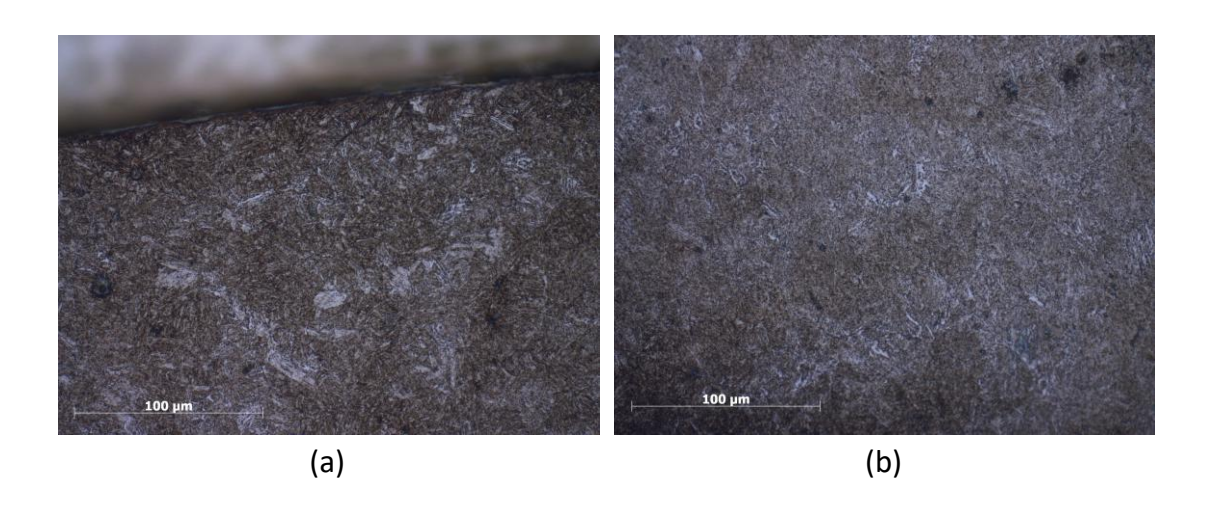


Figure 5.1 Microstructure of AISI 4140 machined a) surface b) bulk



Figure 5.2 Microstructure of AISI 4140 machined and stress relief annealed a) surface b) bulk

There is no substantial visible difference between the microstructures in Figure 5.1 and Figure 5.2. However, with machine samples, the white layer is apparent. Micro hardness measurements from the bulk as Table 5.1 states that there are no significant mechanical properties which occur due to heat treatment. Mechanical properties of AISI 4140 machined and stress relief annealed samples have similar mechanical properties.

Another explanation for residual curve change from hook form is that the machining process is carried out at a low cutting speed. The initial cutting speed was determined to be $230 \, \text{m/min}$ based on the literature. However, due to machining capacity constraints and an 8mm diameter, the maximum cutting speed that could be achieved was $100 \, \text{m/min}$. This lower V_c is beyond the limitation of models capability.

Stress relief annealing for AISI 4140 was effective, resulting in negligible residual stresses in the material. Unfortunately, materials fail location their threads. There might be numerous explanations for this cause.

- Residual stress may not be relieved evenly across threads.
- After relieving residual stresses from samples, the stress concentration effect is prioritized, which may result in increased stress concentration at the tread bottom.
- Stress relief annealing uses a nitrogen atmosphere with oxygen, resulting in surface oxidation. This may have an impact on such types of failures.

During fatigue testing of AISI 4140, corrosion pits were discovered within the machined surface of AISI 4140 samples. This may affect the homogeneity of stress concentrations inside the machined surface. This occurs owing to the material's oxidation affinity. To manage this, researchers were instructed to dip samples in machining liquid to avoid rusting.

The modelling of residual stresses for 316L stainless steel was subjected to the identical circumstances as for AISI 4140. 316L SS is machined at a very low cutting speed of 70m/min. Initially, machining was scheduled to take place at a rate of 110 m/min. Several factors happened during machining, including machining and vibration difficulties, which required reducing the cutting speed to 70 m/min. This low velocity has caused a buildup of edge within the tool. There are two options for modelling accumulation edges.

- 1. Extract build-up edge geometry from tool and perform the modelling
- 2. Adjust friction which corelate with the cutting velocity

Taking practicality into account, the friction coefficient and heat partition coefficients were changed in proportion to cutting speed. The model was unable to include vibration, which might be one of the reasons why the shape of residual stress curves of the machined sample were not accurately predicted.

Stress relief annealing was done on 316L stainless steel, however only about half of the residual stresses were relieved. Stress relief annealing proved difficult to execute in 316L SS because of its susceptibility to sensitization. For the reduction of residual stresses from 316L SS, temperatures more than 850 C are required, although this may damage the sample's microstructure. Clear oxides were also found on the surface of the 316L SS material.

Initial condition	Machined	Machined and heat treated
(0.3 HV)	(0.3 HV)	(0.3 HV)
250	191.1	187.1

Table 5.2 Microhardness measurements of 316L SS

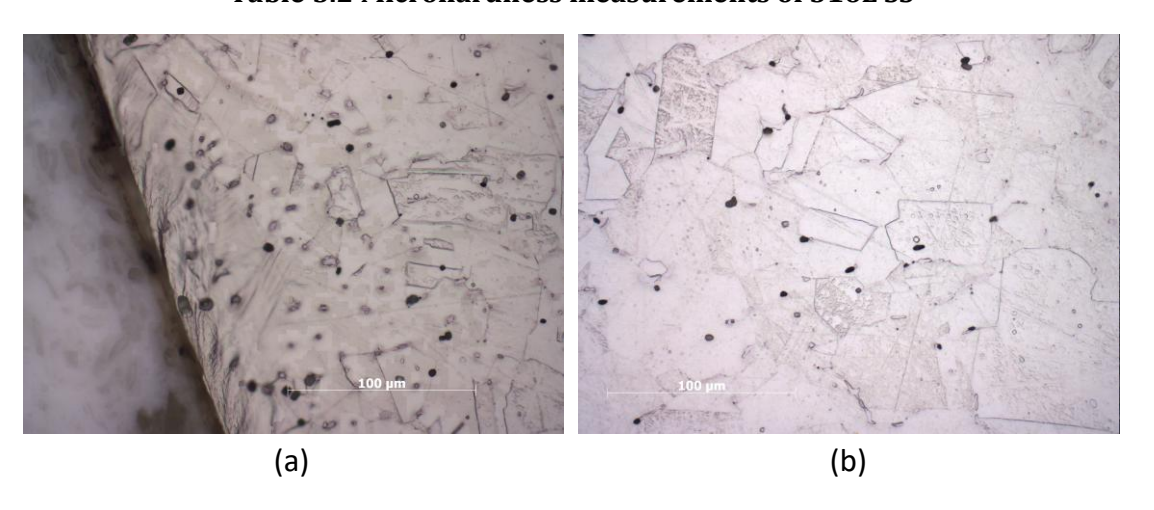


Figure 5.3 Microstructure of 316L SS machined and stress relief annealed

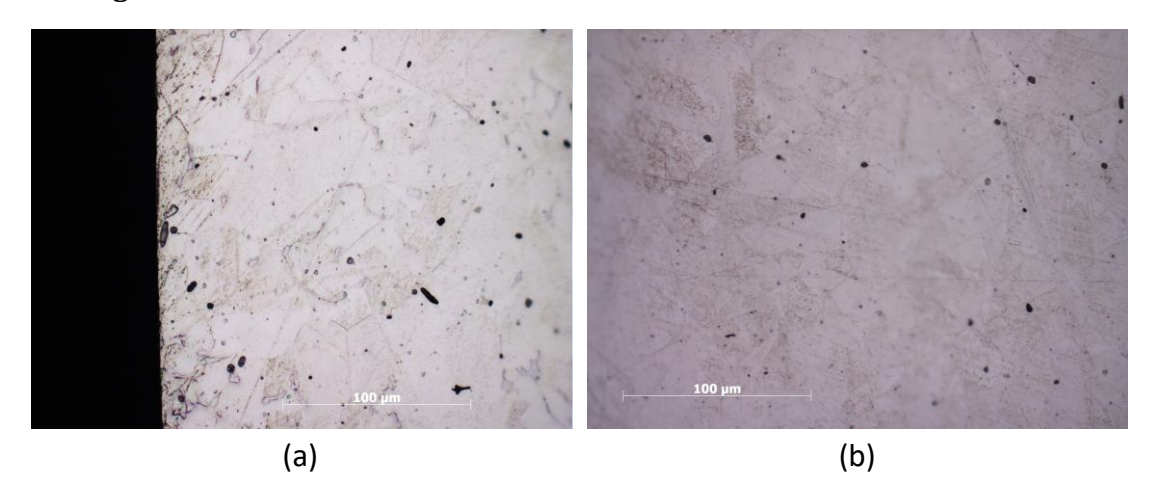


Figure 5.4 Microstructure of 316L SS of machined

Microhardness comparisons reveal that stress relief annealing affects material mechanical properties, however there is no mechanical difference between machined

and heat-treated samples. And the microstructure of 316L machined and heat-treated samples is same, indicating that there is negligible metallurgical change between the two sets of samples.

Self-heating was detected in 316L SS materials during fatigue testing, including machined and stress relief annealed samples. Heat dissipation caused by straining is high in 316L SS material, and the material's limited thermal conductivity prevents heat from dissipating and storing inside the material, resulting in material heating. A similar phenomenon is observed in materials testing during low cycle fatigue testing. To avoid this effect, materials must be subjected to fatigue loading at a low frequency, such as 10 Hz, and a high load ratio.

Chapter 6

Conclusion

A series of tests were undertaken to attain controlled geometrical and metallurgical characteristics for each sample while altering residual stresses. Residual stresses are validated and subjected to experimental fatigue testing to analyse the impact of groove-scale residual stresses on fatigue life.

Stress relief annealing eliminated residual stresses induced by machining in AISI 4140 and diminished residual stresses in 316L stainless steel by 50%. Stress relief annealing successfully attained equivalent mechanical and metallurgical characteristics in both machined and heat-treated samples of 316L and AISI 4140.

A two-scale method to model 3D residual stress proved successful in capturing residual stresses caused by machining. Errors between models and tests can be reduced by considering phenomena such as build up edge phenomena, vibration occur during machining and affected layer.

Fatigue testing findings demonstrate that cracks in machined samples originate in the troughs of the grooves and travel throughout the valley. The fracture results from machining imperfections, namely those present in the valley of the groove.

Pits were discovered in AISI 4140 machined samples, and the generated FEA model revealed that microscale pits did not affect fatigue results or stress concentration on the surface.

The findings of the fatigue tests indicate that machined and heat-treated samples exhibit greater fatigue strength than only machined samples. This confirms that materials exhibiting elevated tensile residual stresses possess diminished fatigue strength.

For future work, AISI 4140 is a material that produces substantial results due to its high machinability, but its corrosion susceptibility must be controlled using stress relief annealing in a vacuum environment. Machined samples require an oxygen-free environment to avoid pit development.

Bibliography

- Abd El Whaab, E. A. M. (2014). COMPARATIVE STUDY ON FRACTURE TOUGHNESS OF STEEL AFTER DIFFERENT THERMAL TREATMENTS. https://www.researchgate.net/publication/345849731
- Aridhi, A., Dumas, M., Perard, T., Girinon, M., Brosse, A., Karaouni, H., Valiorgue, F., & Rech, J. (2022). 3D Numerical modelling of turning-induced residual stresses in 316L stainless steel. *Procedia CIRP*, 108, 885–890. https://doi.org/10.1016/j.procir.2022.07.001
- Arola, D., & Williams, C. L. (2002). Estimating the fatigue stress concentration factor of machined surfaces. *International Journal of Fatigue*, *24*(9), 923–930. https://doi.org/10.1016/S0142-1123(02)00012-9
- ASTM Special Technical Publication. (1949). ASTM Special Technical Publication.
- Badaruddin, M., Sugiyanto, Wardono, H., Andoko, Wang, C. J., & Rivai, A. K. (2019). Improvement of low-cycle fatigue resistance in AISI 4140 steel by annealing treatment. *International Journal of Fatigue*, 125, 406–417. https://doi.org/10.1016/j.ijfatigue.2019.04.020
- Beaumont, P., Guérin, F., Lantieri, P., Facchinetti, M. L., & Borret, G. M. (2012). Accelerated fatigue test for automotive chassis parts design: An overview. *2012 Proceedings Annual Reliability and Maintainability Symposium*, 1–6.
- Berry, L., Wheatley, G., Ma, W., Masoudi Nejad, R., & Berto, F. (2022). The influence of milling induced residual stress on fatigue life of aluminum alloys. *Forces in Mechanics*, 7. https://doi.org/10.1016/j.finmec.2022.100096
- Chao, Q., Thomas, S., Birbilis, N., Cizek, P., Hodgson, P. D., & Fabijanic, D. (2021). The effect of post-processing heat treatment on the microstructure, residual stress and mechanical properties of selective laser melted 316L stainless steel. *Materials Science and Engineering: A, 821*. https://doi.org/10.1016/j.msea.2021.141611
- Chomienne, V., Valiorgue, F., Rech, J., & Verdu, C. (2023). Development of a surface engineering strategy to quantify the sensitivity of surface integrity features in fatigue performance. *Proceedings of the Institution of Mechanical Engineers, Part B:*

- Journal of Engineering Manufacture, 237(4), 561–572. https://doi.org/10.1177/09544054221109110
- Dumas, M., Fabre, D., Valiorgue, F., Kermouche, G., Van Robaeys, A., Girinon, M., Brosse, A., Karaouni, H., & Rech, J. (2021a). 3D numerical modelling of turning-induced residual stresses A two-scale approach based on equivalent thermo-mechanical loadings. *Journal of Materials Processing Technology*, 297. https://doi.org/10.1016/j.jmatprotec.2021.117274
- Dumas, M., Fabre, D., Valiorgue, F., Kermouche, G., Van Robaeys, A., Girinon, M., Brosse, A., Karaouni, H., & Rech, J. (2021b). 3D numerical modelling of turning-induced residual stresses A two-scale approach based on equivalent thermo-mechanical loadings. *Journal of Materials Processing Technology*, 297. https://doi.org/10.1016/j.jmatprotec.2021.117274
- Dumas, M., Kermouche, G., Robaeys, A. Van, Karaouni, H., & Rech, J. (2021). *Turning-induced surface integrity for a fillet radius in a 316L austenitic stainless steel*.
- Ee, K. C., Dillon, O. W., & Jawahir, I. S. (2005). Finite element modeling of residual stresses in machining induced by cutting using a tool with finite edge radius. *International Journal of Mechanical Sciences*, 47(10), 1611–1628. https://doi.org/10.1016/j.ijmecsci.2005.06.001
- Elangeswaran, C., Cutolo, A., Muralidharan, G. K., de Formanoir, C., Berto, F., Vanmeensel, K., & Van Hooreweder, B. (2019). Effect of post-treatments on the fatigue behaviour of 316L stainless steel manufactured by laser powder bed fusion. *International Journal of Fatigue*, 123, 31–39. https://doi.org/10.1016/j.ijfatigue.2019.01.013
- Enomoto, Y. (2022). Steam turbine retrofitting for the life extension of power plants. In *Advances in Steam Turbines for Modern Power Plants* (pp. 491–530). Elsevier. https://doi.org/10.1016/B978-0-12-824359-6.00008-1
- Fajdiga, G., & Sraml, M. (2009). Fatigue crack initiation and propagation under cyclic contact loading. *Engineering Fracture Mechanics*, 76(9), 1320–1335. https://doi.org/10.1016/j.engfracmech.2009.02.005
- Field, M. and K. J. F. and others. (1971). Review of surface integrity of machined components. *Annals of the CIRP*, 20, 153–163.
- Gerstenmeyer, M., Zanger, F., & Schulze, V. (2018). Influence of Complementary Machining on fatigue strength of AISI 4140. *CIRP Annals*, 67(1), 583–586. https://doi.org/10.1016/j.cirp.2018.04.103

- Guo, Y. B., & Liu, C. R. (2002). FEM Analysis of Mechanical State on Sequentially Machined Surfaces. In *Machining Science and Technology* (Vol. 6, Issue 1).
- Gür, C. H., & Arda, E. B. (2003). Effect of tube spinning and subsequent heat treatments on strength, microstructure and residual stress state of AISI/SAE type 4140 steel.

 *Materials Science and Technology, 19(11), 1590–1594. https://doi.org/10.1179/026708303225008022
- Han, S., Cici, M., Pascal, H., Valiorgue, F., & Rech, J. (2024). 3D residual stress modeling in turning of AISI 4140 steel. https://hal.science/hal-04398176
- Hu, Y., Chen, Y., He, C., Liu, Y., Wang, Q., & Wang, C. (2020). Bending fatigue behavior of 316L stainless steel up to very high cycle fatigue regime. *Materials*, *13*(21), 1–15. https://doi.org/10.3390/ma13214820
- Januário Cordeiro Gomes, D., Sales Palma, E., & Américo Almeida Magalhães Júnior, P. (2015). Influence Of Surface Roughness On Ultra-High-Cycle Fatigue Of Aisi 4140 Steel. In *Journal of Engineering Research and Applications www.ijera.com* (Vol. 5). www.ijera.com
- Javidi, A., Rieger, U., & Eichlseder, W. (2008). The effect of machining on the surface integrity and fatigue life. *International Journal of Fatigue*, *30*(10–11), 2050–2055. https://doi.org/10.1016/j.ijfatigue.2008.01.005
- Jawahir, I. S., Brinksmeier, E., M'Saoubi, R., Aspinwall, D. K., Outeiro, J. C., Meyer, D., Umbrello, D., & Jayal, A. D. (2011). Surface integrity in material removal processes: Recent advances. CIRP Annals - Manufacturing Technology, 60(2), 603–626. https://doi.org/10.1016/j.cirp.2011.05.002
- Jouini, N., Revel, P., & Thoquenne, G. (2020). Influence of surface integrity on fatigue life of bearing rings finished by precision hard turning and grinding. *Journal of Manufacturing Processes*, 57, 444–451. https://doi.org/10.1016/j.jmapro.2020.07.006
- Kermouche, G., Aleksy, N., Loubet, J. L., & Bergheau, J. M. (2009). Finite element modeling of the scratch response of a coated time-dependent solid. *Wear*, *267*(11), 1945–1953. https://doi.org/10.1016/j.wear.2009.05.005
- Limodin, N., & Verreman, Y. (2006). Fatigue strength improvement of a 4140 steel by gas nitriding: Influence of notch severity. *Materials Science and Engineering: A, 435–436*, 460–467. https://doi.org/10.1016/j.msea.2006.07.034

- Liu, C. R., & Guo, Y. B. (2000). Finite element analysis of the effect of sequential cuts and tool–chip friction on residual stresses in a machined layer. *International Journal of Mechanical Sciences*, 42(6), 1069–1086. https://doi.org/10.1016/S0020-7403(99)00042-9
- Lurdos, O. (2008). N° d'ordre : 478 SGM THÈSE présentée par Lois de comportement et recristallisation dynamique : approches empirique et physique Soutenue à Saint-Étienne le lundi 28 avril 2008.
- Majzoobi, G. H., & Daemi, N. (2010). The effects of notch geometry on fatigue life using notch sensitivity factor. *Transactions of the Indian Institute of Metals*, 63(2–3), 547–552. https://doi.org/10.1007/s12666-010-0080-3
- Menig, R., Schulze, V., & Vöhringer, O. (2002). Residual stress stability and alternating bending strength of AISI 4140 after shot peening and successive annealing.

 Materials Science Forum, 404–407, 469–476.

 https://doi.org/10.4028/www.scientific.net/msf.404-407.469
- Meyer, K., Denkena, B., Breidenstein, B., & Abrão, A. M. (2020). Influence of residual stress depth distribution on lifecycle behaviour of AISI4140. *Procedia CIRP*, *87*, 450–455. https://doi.org/10.1016/j.procir.2020.02.064
- Mondelin, A., Rech, J., Feulvarch, E., & Coret, M. (2014). Characterisation of surface martensite-austenite transformation during finish turning of an AISI S15500 stainless steel. *International Journal of Machining and Machinability of Materials*, *15*, 101–121. https://doi.org/10.1504/IJMMM.2014.059190ï
- Mondelin, A., Valiorgue, F., Rech, J., Coret, M., & Feulvarch, E. (2012). Hybrid model for the prediction of residual stresses induced by 15-5PH steel turning. *International Journal of Mechanical Sciences*, 58(1), 69-85. https://doi.org/10.1016/j.ijmecsci.2012.03.003
- Nasr, M. N. A., Ng, E.-G., & Elbestawi, M. A. (2007). Modelling the effects of tool-edge radius on residual stresses when orthogonal cutting AISI 316L. *International Journal of Machine Tools and Manufacture*, 47(2), 401–411. https://doi.org/10.1016/j.ijmachtools.2006.03.004
- Novovic, D., Aspinwall, D. K., Dewes, R. C., Bowen, P., & Griffiths, B. (2016). The effect of surface and subsurface condition on the fatigue life of Ti–25V–15Cr–2Al–0.2C %wt alloy. *CIRP Annals Manufacturing Technology*, 65(1), 523–528. https://doi.org/10.1016/j.cirp.2016.04.074

- Parida, B. K. (2001). Fatigue Testing. In *Encyclopedia of Materials: Science and Technology* (pp. 2994–2999). Elsevier. https://doi.org/10.1016/B0-08-043152-6/00533-7
- Philip, A. M., & Chakraborty, K. (2022). Some studies on the machining behaviour of 316L austenitic stainless steel. *Materials Today: Proceedings*, *56*, 681–685. https://doi.org/https://doi.org/10.1016/j.matpr.2022.01.132
- Ruiz De Eguilaz, E., Rech, J., & Arrazola, P. (2010). Characterization of friction coefficient and heat partition coefficient between an AISI4140 steel and a TiN-coated carbide Influence of (Ca, Mn, S) steel's inclusions. *Proceedings of the Institution of Mechanical Engineers, Part J: Journal of Engineering Tribology*, 224(10), 1115–1127. https://doi.org/10.1243/13506501JET818
- Samant, A., & Maity, K. P. (n.d.). A THESIS SUBMITED IN PARTIAL FULFILLMENT OF THE REQUIRMENT FOR THE DEGREE OF Master of technology In Mechanical Engineering Under the supervision of.
- Santecchia, E., Hamouda, A. M. S., Musharavati, F., Zalnezhad, E., Cabibbo, M., El Mehtedi, M., & Spigarelli, S. (2016). A Review on Fatigue Life Prediction Methods for Metals. In *Advances in Materials Science and Engineering* (Vol. 2016). Hindawi Limited. https://doi.org/10.1155/2016/9573524
- Shet, C., & Deng, X. (2003). Residual stresses and strains in orthogonal metal cutting. International Journal of Machine Tools and Manufacture, 43(6), 573–587. https://doi.org/10.1016/S0890-6955(03)00018-X
- Smith, W. F. (1993). Structure and properties of engineering alloys. *New York: McGraw Hill, 2nd,* 156.
- Susmel, L. (2009). Useful stress quantities used in fatigue problems. In *Multiaxial Notch Fatigue* (pp. 1–32). Elsevier. https://doi.org/10.1533/9781845695835.1
- Ulutan, D., & Ozel, T. (2011). Machining induced surface integrity in titanium and nickel alloys: A review. In *International Journal of Machine Tools and Manufacture* (Vol. 51, Issue 3, pp. 250–280). https://doi.org/10.1016/j.ijmachtools.2010.11.003
- Vernon, P. J., & Mackin, T. J. (2001). Fatigue failure analysis of a leg press exercise machine. In *Failure Analysis Case Studies II* (pp. 255–266). Elsevier. https://doi.org/10.1016/B978-0-08-043959-4.50026-2